Catalysis Today 144 (2009) 185–200

Contents lists available at ScienceDirect

Catalysis Today

journal homepage: www.elsevier.com/locate/cattod

Conversion of hydrocarbon fuels to syngas in a short contact time catalytic reactor

L. Bobrova *, N. Vernikovskaya, V. Sadykov

Boreskov Institute of Catalysis, Novosibirsk 630090, Russia

ARTICLE INFO

Article history:
Available online 4 March 2009

Keywords:
Syngas formation
Methane
Isooctane
Gasoline
Monolith reactor
Radial-flow reactor
Thermodynamics
Dynamic simulations

ABSTRACT

Some results of the theoretical and experimental research on the oxidative production of syngas from hydrocarbon fuels in catalytic reactors which operate at high temperatures and short contact times are presented. Pilot scale tests of the partial oxidation of methane, isooctane and gasoline have been carried out in nearly adiabatic conditions on structured catalysts developed at the Boreskov Institute of Catalysis and characterized by a low (≤0.5 wt./wt.%) content of noble metals. High yield of syngas and stable performance of the catalysts were revealed in the experiments. The details of interaction between chemical and physical processes inside adiabatic monolith reactor have been elucidated by mathematical modeling of the partial oxidation reaction on the base of catalyst detailed chemistry. The problems that emerged from the short contact time reactor operating on a pilot scale are also discussed.

1. Introduction

Hydrogen combustion and oxidation are pollution free and supply sufficient energy for transportation and other applications. This makes hydrogen a major candidate to meet the world energy demand. However, this simplest element and most plentiful gas in the universe does not exist alone in the nature. It always combines with other elements such as oxygen and carbon. Natural gas contains hydrogen (about 95% of natural gas is methane), as do biomass and hydrocarbons. Nowadays, almost all the hydrogen manufactured on a large scale is obtained by steam reforming of hydrocarbons. For the near term, this method of production will continue to dominate, although several other methods have been developed [1–5].

To avoid a hydrogen supply infrastructure and eliminate gaseous H_2 storage issues, production of hydrogen by the small-scale processing of conventional fuels near the end-user is considered to be a good solution. Catalysis offers a variety of options for the conversion of hydrocarbon fuel into hydrogen-rich gas. One of the most effective methods of generating hydrogen from hydrocarbon fuels is fuel reforming to produce synthesis gas or syngas (H_2 + CO). Generally, the primary fuel is converted into synthesis gas with air and (or) steam on a catalyst at high temperatures using one of three major techniques: steam reforming, partial oxidation, and autothermal reforming [6]. Synthesis gas production by steam reforming is not feasible for the small-scale processing, because steam reformers are large and expensive plants that can hardly be scaled down. A considerable disadvantage of the steam reforming process is that it is an endothermic reaction. When discussing the three principal pathways, Ahmed and Krumpelt [7] demonstrate that the partial oxidation (direct partial oxidation where the feed reacts directly with air or enriched air with carefully balanced oxygen-to-fuel ratios) and autothermal reforming (indirect partial oxidation, as a combination of partial oxidation and steam reforming in stand-alone catalytic system) processes are more attractive for the small-scale practical applications. Contrary to widely held beliefs, these processes are also capable of higher reforming efficiencies than steam reforming. The gross oxidative reaction of syngas formation from a general fuel (hydrocarbon or oxygenate) can be described by the following expression:

$$C_nH_mO_p + x\,O_2 + (n - 2x - p)H_2O = n\,CO + (n - 2x - p + (1/2)\,m)H_2$$

The process is carried out in the presence of a catalyst which controls the product composition. Since the first publications [8–10], there has been a significant interest in the new catalytic processes that operate at high temperatures and under short contact times over structured catalysts. It has been shown that catalytic partial oxidation of methane provides close to 100% methane conversion and >90% synthesis gas yields in millisecond contact times. Compared to contact times of seconds in a steam

* Corresponding author at: Boreskov Institute of Catalysis, Pr. Ak. Lavrentieva, 5, Novosibirsk 630090, Russia. Tel.: +7 3833269438.
E-mail address: lbobrova@catalysis.ru (L. Bobrova).

0920-5861/$ – see front matter © 2009 Elsevier B.V. All rights reserved.
doi:10.1016/j.cattod.2009.01.034

reformer, the reactors can be three orders of magnitude smaller processing the same amount of synthesis gas. The authors could exclude the contribution of thermal either nonoxidative or oxidative pyrolysis on the basis of the high conversion achieved. Low coking was attributed to the fact that carbon-producing reactions (olefin cracking, Boudouard reaction, etc.) did not approach an equilibrium and that the presence of CO_2 and H_2O favored reforming of the carbon formed [10,11].

Structured catalysts are ceramic and metallic configurations which constitute both the catalyst support and the reactor. According to classification of Cybulski and Moulijn [12], there are three basic types:

- monoliths, in the form of continuous unitary structures (e.g. honeycombs, foams or interconnected fibers) containing small passages with the walls loaded with catalytically active agents;
- membrane catalysts—structures with permeable walls between passages, thus allowing selective transport of reactants or products; and
- arranged catalysts, which are either arrays of particles or sheets superimposed, to allow crossflow.

Recent literature on partial oxidation reactions shows that there is a growing need to extend our conventional catalyst and reaction engineering knowledge base to this new reactor category, to have better understanding of flow contacting, multispecies transports and detailed reaction kinetics and their interactions in monolith reactors, to have improved understanding of reactor structure impact and materials (washcoat) influence on the catalyst performance [12–16]. The oxidation processes in the monolith reactor exhibit features not observed in conventional packed bed reactors. Indeed, due to the very high efficiency of the catalyst in such configurations, the structured catalysts operate at 800–1200 °C with the gas flow velocities of ca. 1 m/s with open channel catalyst structures for effective contact times of a few milliseconds. The process is autothermal and nearly adiabatic one. Preheating the feed enhances syngas selectivity, but no reactor preheat was often necessary other than that required to vaporize the fuel [17,18]. While the basic feasibility of the high-temperature catalytic oxidation reactions has been sufficiently demonstrated, many obstacles still remain to be solved on the way to an industrial application. In spite of the numerical research in this area, the performance targets for the fuel processing in the small scale still require the development of a catalyst which exhibits a high activity along with thermal and mechanical stability for the process. It also requires detailed thermodynamic and kinetic information about the reaction. Although the hydrocarbon reforming reactions proceed quickly and equilibrate rapidly, both radial and axial temperature gradients may arise in monolith reactors. The spatial distribution of temperature in the reactor results from the interplay of kinetics, hydrodynamics, heat transfer and process parameters [14,19,20].

This paper briefly reviews general results of the combined experimental and modeling investigation efforts currently being performed at the Boreskov Institute of Catalysis on the development of both the structured catalysts and technology for syngas production from hydrocarbon fuels in the axial and radial type reactors. The following scientific and technical approaches have been applied in the research and development program:

- synthesis of nanocrystalline active components comprising ceria-zirconia fluorite-like complex oxides promoted with small amount of noble metals was carried out to ensure conversion of hydrocarbons into syngas via a highly efficient route of pyrolysis-direct oxidation that depends on (a) ability of dispersed noble metals to dissociate hydrocarbons generating reactive C_xH_y and H_2, and (b) mobility and reactivity of surface oxygen (hydroxyl groups) which are rapidly transferred to the metal particle-support oxides interface where they consume the surface C_xH_y-particles producing syngas;
- monolithic catalysts were developed by supporting the synthesized nanocrystalline active components onto the corundum and metallic substrates;
- thermodynamic equilibrium restrictions on the operational parameters have been outlined on the base of thermodynamic simulations;
- pilot scale experiments in structured reactors operated under nearly adiabatic conditions have been carried out;
- transient behavior of the monolith reactor during start-up (ignition) of the methane partial oxidation to synthesis gas over Pt/Ce–Zr–La catalyst has been studied in detail both experimentally and by simulation via mathematical modeling, thus providing the necessary bases for theoretical optimization of the catalyst-bed configuration and process parameters.

2. Experimental

2.1. Catalysts preparation and characterization

High-performance active components of the catalysts for selective oxidation of hydrocarbons (gaseous and liquid) into syngas at short contact times comprising nanocrystalline ceria–zirconia solid solutions doped by La, Pr, etc., and promoted with a small amount of noble metals (not higher than 0.5%) have been developed at the Boreskov Institute of Catalysis. The data of various physicochemical, kinetic and mechanistic investigations of the Pt/ceria (ceria–zirconia)-based materials in methane partial oxidation are reported elsewhere [21–36]. Ceria-based mixed oxides ($Ce_xM_{1-x}O_y$) are versatile solid oxygen exchangers. These materials have been investigated since the early 1990. Incorporation of zirconium into the ceria lattice creates a high concentration of defects improving, thus, the oxygen mobility and oxygen storage capacity [37]. At high (400–800 °C) temperatures, the redox cycle $Ce^{3+} \Rightarrow Ce^{4+} + e^-$ facilitates oxygen storage and release from the bulk fluorite lattice. When combined with noble or non-noble metal particles, this makes them ideal candidates for catalytic oxidation applications such as partial oxidation of hydrocarbons into syngas [25].

The high-dispersed homogeneous solid ceria–zirconia solutions were synthesized by using the polymeric polyester precursors decomposition techniques [24,33,38]. Nanoparticles of active metals or their perovskite-like precursors of $LaPt(Ni)O_3$ and $LaPt(Ru)O_3$ type were supported via wet impregnation with the mixed solutions of chloride-free salts [24,26,33]. Reactivity and diffusion mobility of the bulk/surface oxygen were studied by using the methods known elsewhere [39–41] and based on oxygen isotope exchange, temperature-programmed reduction by carbon monoxide, methane and hydrogen in microcatalytic facilities.

The different types of fuel processing catalysts were fabricated:

Microspherical LaNiPt (9 wt.%)/Ce–ZrOx (ca. 12 wt.%)/γ-Al_2O_3 catalyst was prepared by wet impregnation of 1 mm diameter γ-Al_2O_3 spheres (BET surface area 150 m^2/g) with the appropriate solutions.

Composite ceramometal monoliths (46 mm diameter, 23 mm length, ca. 300 cpsi channel density, ca. 0.3 porosity). The raw materials were Cr-Al alloy powder and CeO_2 powder (40 wt.%, prepared by decomposition of nitrate). To form a set of transport channels, easily burned organic fibers were inserted into the cermet matrix before the hydrothermal treatment stage (HTT) [26–28,33,41]. A row of parallel passageways (ca. 0.5 mm diameters) along the substrate monolith are inter-

connected by narrow (ca. 0.1 mm) anfractuous channels separated by ca. 0.05 mm walls. The mixture of Cr–Al alloy and CeO_2 loaded into a special die was subjected to HTT at 200 °C followed by calcination in air at 900–1200 °C. Platinum and $LaNiO_3$ as basic active components were introduced by using the incipient wetness impregnation procedure followed by drying and calcination in air at 900 °C. The inlet part of a monolith was promoted by Rh or Ru + La in two additional impregnations with corresponding solutions followed by drying and calcination.

Metallic monoliths. For catalysts based upon thermal conducting metallic substrates (diameter 55 mm, length 45 mm, specific surface area 4700 m^2/m^3, porosity ca. 0.8), the first preparation stage includes supporting a thin (ca. 5–10 microns) protective corundum sublayer on a fecraloy foil (50–100 micron thickness) by blast dusting technique [28,33]. Monolithic substrates are obtained via stacking a flat and corrugated foils and winding them into an Archimedes spiral. Secondary Ce–Zr–La–O mixed oxide support is coated via a standard washcoating procedure using an alumina hydroxide as a binder. LaNiPt (ca. 1 wt.%) and LaRu (ca. 1 wt.%) active components were successively supported via wet impregnation followed by drying and calcination at 900°C.

The gauze configuration LaCeZrOx (5.3 wt.%)/LaNiPt (2 wt.%)/fecraloy catalyst was prepared by a technique that involves blast dusting of a corundum layer on the gauze substrate (woven from the fecraloy wires with diameter 2.0 mm and ca. 0.2 mm spacing) followed by supporting γ-Al_2O_3 (3.6 wt.%) from an appropriate suspension. The corresponding active phase was formed by the deposition of $LaCeZrO_x$ from a suspension followed by the wet impregnation of LaNiPt from an appropriate solution.

Radial-flow monolith consisted of 60 catalytic washers (outer diameter 38 mm, inner diameter 19, height 2 mm) piled up in a cylinder by means of nut bolting. Multiple radial channels (0.5 mm depth and 0.5 mm width) were milled in the washer planes with the angular step width of 4 degrees, resulting in 90 channels on a side. Protective layer of alumina on the fecraloy washers was supported by blast dusting. The catalytically active $LaNi_{0.9}Pt_{0.1}/CeZrO_x$ composition was supported on the protective layer using the same procedures as for metallic foil monoliths.

Ceramic monoliths (hexagonal side 28 mm, monolith length 50 mm, wall thickness 0.25 mm, equivalent channel diameter 1.9 mm, surface area 3–10 m^2/g) based on the extruded low-surface area corundum substrate were prepared by supporting $LaNiO_3$/Ce–Zr–La–O oxides (up to 15 wt.%) and Pt (up to 0.5 wt.%) with the impregnation procedures followed by drying and calcinations as described in [33].

2.2. Reactor set-up and experimental procedure

The type of a catalyst determines the design of a structured reactor and feed preparation/supply system for the small-scale application [42–45]. In this paper two different reactor configurations have been tested under autothermal conditions, one is an axial type monolith reactor, and the other is a radial-flow type reactor.

Monolith reactor. The apparatus and procedures for oxidative reformation of such fuels like methane, isooctane and gasoline in the monolith reactors have been described elsewhere [31–36]. In general, the experiments were carried out in a tubular quartz reactor, approximately 300 mm long and with 60 mm inner diameter. The quartz tube was surrounded by an insulation material and immersed into a stainless steel reactor of a bigger size. Catalytic monoliths (composite ceramometal, ceramic, or metallic monoliths) were placed inside. Unloaded monoliths, the 10 mm long fragments of an extruded corundum monolith with 1.9 mm hydraulic diameter of its channels, were placed in front of and behind the catalytic monoliths to reduce radiation heat loss. Chromel–alumel thermocouples were used to monitor the temperature at various positions along the reactor length. The entire reactor ran autothermally at atmospheric pressure. The product composition was determined by gas chromatography (TCD, FID). A fraction of product gas was taken immediately beyond the monoliths package. The fuel feed was delivered to the reactor through a stainless steel tube of 28 mm ID and 1.5 m height filled with inert porcelain rings. The tube was placed inside a fluidized bed heater-thermostat to ensure the uniform temperature profile along the tube. The total flow rate of the feed (fuel, air, and steam) to the reactor was varied between 3.5 and 11 m^3/h (STD). The feed stoichiometry is given as the oxygen to carbon ratio (O_2/C), which is defined as the moles of dioxygen divided by the moles of carbon in the feed, and water-to-carbon ratio (H_2O/C), which is defined as the moles of water divided by the moles of carbon in the feed. To ignite the reaction, the feed flow was fed into preheated (by air at ~300 °C) reactor. In the case of methane reformation, heating tape was used to heat additionally the reactor walls to the temperature of about 500 °C. The experimental data are compared with the results of thermodynamic modeling.

Autothermal radial-flow reactor. The integrated reactor concepts are currently the focus of intense research in reactor engineering. In these concepts, different unit operations such as heat exchange, distributed feed supply, or product separation are integrated in addition to the chemical reaction into one multifunctional apparatus by energy saving design [46].

A promising approach of the multifunctional reactor concepts employing recuperative heat exchange between the process streams and "entering and leaving energy and species along the full length of the apparatus" [46] was utilized in the radial-flow reactor configurations developed for the partial oxidation of natural gas to synthesis gas. It is known that the successful operation of a radial-flow reactor lies mainly in the details of the mechanical design, which is more complicated than that of a monolith reactor [47]. The autothermal radial-flow reactor system (see Fig. 1) includes a multiple catalyst-beds cylindrical architecture corresponding to a total volume of about 577.2 cm^3 (radial-flow monolith 106.3 cm^3, gauze catalyst-bed 134.0 cm^3, microspherical catalyst-bed 336.9 cm^3) and heat exchanger disposed about the reactor as an outer shell having a passage therethrough, wherein the air–methane mixture travels through the passage for preheating the feed gas, using the hot gases leaving the radial multiple catalyst-beds, prior to entering the reactor axis chamber with blocked outlet. Thus the feed is forced throughout the catalyst-beds in radial direction. A schematic drawing of the radial-flow reactor catalyst-beds with approximate positions of the thermocouples is shown in Fig. 2. The radial-flow monolith (a stack of the catalytic washers) 125 mm long was wrapped in the catalytic gauze, and then microspheroidal catalyst was gently loaded into a space between the gauze bed and an outer retention mesh. The catalytic arrangement was held between two flanges placed on the edges of the arrangement to ensure a good seal and eliminate bypass flow of the reformate mixture.

During start-up period, an external heater was applied to heat up the reactor by air to ca. 450 °C. Once an operational temperature was achieved, the feed (29 v/v% natural gas in air) with a flow rate of 2 m^3/h (STD) was fed at 425 °C into the preheated reactor for enabling thus its quick start-up. In the stationary operation mode, the inlet mixture at an ambient temperature was introduced into the heat exchanger for preheating prior to entering the central part of the reactor. Further, the preheated feed was distributed along axis of the reactor and flowed in the radial direction across the

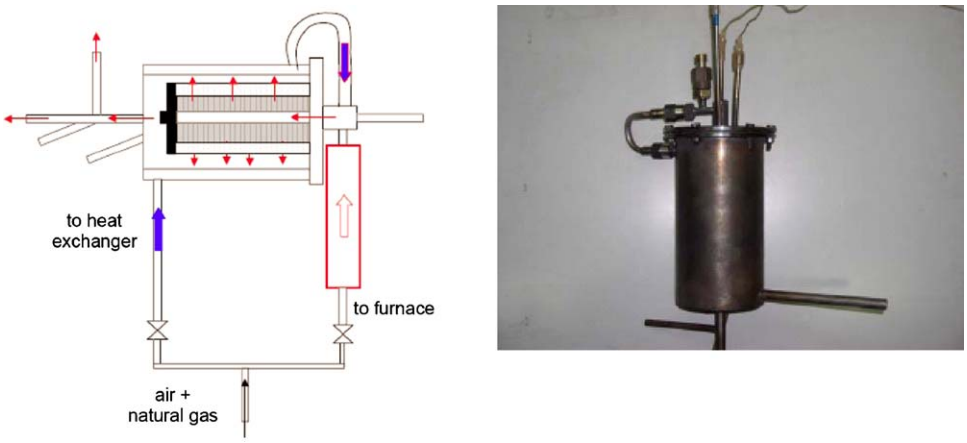

Fig. 1. Autothermal radial-flow reactor configuration.

catalyst-beds. Thus, the velocity of the gas is highest at the inlet and then decreases as the gas fluid moves away from the inlet of the reactor. The reformed gas was collected into a plenum around the catalyst arrangement and exited from a single pipe. In this work, this reactor was tested at the same natural gas–air ratio of about 0.33 in the feed with flow rate varied from 4.3 to 14.4 m^3/h.

The gas probes were taken at the input and output of the reactor to be analyzed by a gas chromatograph. H_2, O_2, N_2, CO, CH_4, and CO_2 concentrations in the gas mixture were directly measured and water concentration was calculated based on atomic mass balance. A ratio of CO to the sum of CO, CO_2 and CH_4 in the product gas carbon monoxide provided the CO selectivity, while a ratio of H_2 to $H_2 + H_2O$ provided the hydrogen selectivity.

3. Results and discussion

3.1. Experimental results

3.1.1. Monolith reactor performance results

Most of the results obtained in the study of syngas generation by air and steam–air conversion of the natural gas, isooctane and gasoline (composition similar to gasoline of grade 92) have been published already [27,28,31–36]. In the paper, we have focused our attention on the process performance being influenced by the monolith type and operating mode.

Composite ceramometal monoliths. When using isooctane as a fuel, the ignition temperature of this catalyst performance was 275 °C [34], while the temperature of about 410 °C was required to light off the reaction of methane partial oxidation [27,28]. For a feed containing 24% of methane in air and at 0.084 s (at STD) contact time, composite ceramometal monolith provides a higher methane conversion combined with a high CO and H_2 yield compared to the honeycomb catalyst on corundum substrate (accordingly, 96, 95, 94% against 84, 91, 87%). This is due to the optimal textural properties of the composite cermet monolith characterized by the high mass transfer rates to the catalytic sites [27,28].

It is known that a catalyst lifetime is limited by thermal stresses and deactivation. A sharp temperature profile over catalytic monolith is often present, because in the presence of oxygen deep oxidation occurring in the front of catalytic monolith is strongly exothermic, whereas with no oxygen in the gas phase the endothermic reactions proceed in the downstream part of the monolith. Moreover, the formation of hotspots may also occur, affecting both stability and safety of the process. A body subjected to a varying temperature field develops thermal stresses. Improved catalyst durability is possible by alleviating axial temperature gradient, which results in thermal stresses [48]. The temperature profile in an adiabatically operated monolith is characteristic of the reforming chemistry, catalytic composition, and structure of the monolith. The cermet monolith support has a higher conductive transfer compared to that for corundum substrate [27,28]. A difference of about 200 °C between the front and back faces of the cermet monolith was detected in the steady state when testing isooctane (Fig. 3, left) and methane [27,28,34], in spite of the fact that the reaction heat evolved in the partial oxidation of isooctane to syngas is higher than that in the methane conversion (see below Section 3.2).

The temperature profile is also affected by variation of the active component composition along the monolith [49,50]. Fig. 3 shows isooctane partial oxidation performance for two different types of catalytic supports: a base composition of 7.8 wt.% LaNiPt/0.87 wt.% LaRu and a base composition with the 0.02 wt.%. Rh loading into ca. 2 mm front part of the cermet monolith. It is found

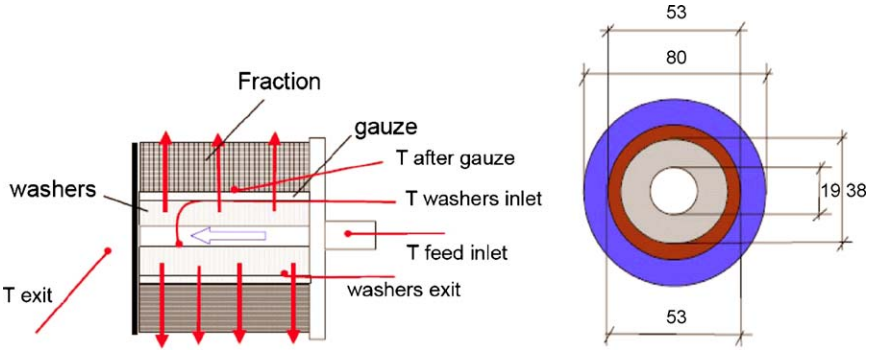

Fig. 2. Schematic drawing the radial-flow reactor catalyst-beds.

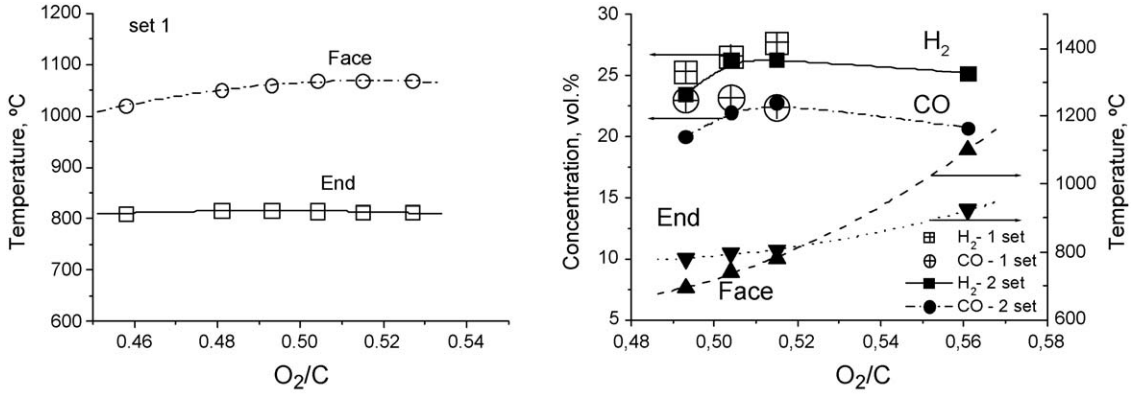

Fig. 3. Isooctane (0.350 kg/h) partial oxidation performed on the composite 7.8 wt.% LaNiPt/0.87 wt.% LaRu/cermet monolith. Figure on the left and open symbols on the right exhibit experimental data in case of 0.02 wt.%. Rh addition on the inlet part of the catalytic monolith (set 1).

that the back-face temperatures respond just a little to the changing of O_2/C ratio in the feed (Fig. 3, left). Addition of Rh into the inlet part of the monolith provides a higher exothermicity of the local reactions in the presence of gas-phase oxygen. However, the product gas composition is determined by thermodynamic equilibrium at the exit temperatures, which are nearly the same for the considered catalytic supports. No C_2–C_3 components were detected in the product gas that can be explained by a minor role of the homogeneous reactions in the cermet monolith geometry. Besides, high thermal stability and mechanical strength make the composite ceramometal monoliths very attractive for practical application.

Metallic monoliths. Radial and axial temperature gradients developed in monoliths may lead to corresponding variations in both catalyst efficiency and selectivity, which are known to be very sensitive to temperature. It is explained by the fact that an increase in temperature favors the intrinsic kinetic constant with respect to diffusional constant [51]. At the fixed fuel flow rate, increasing O_2/C molar ratio in the feed enhances exothermic reactions in the reforming process. Heat conduction in the metallic supports of structured catalysts can provide an effective alternative mechanism to remove the heat generated by the strongly exothermic reactions and supply the reaction heat to the endothermic reactions, thereby providing a moderating effect on the catalyst temperature (Fig. 4).

For this type of monoliths, both partial oxidation and autothermal reforming processes of methane, isooctane and gasoline have been investigated experimentally [31–36]. The monolith reactor exit data showing the product gas species in the gasoline partial oxidation and adiabatic temperature rise are presented in Fig. 5. The two metallic monoliths operate in good approximation adiabatically for all O_2/C ratios studied experimentally. The equilibrium curves for the species concentrations and adiabatic temperature rise at the exit temperature and constant pressure (101.325 kPa) have been determined by calculations of thermodynamic equilibria with a model gasoline fuel (see Section 3.2 below). Fair qualitatively and quantitatively, the experimental data follow the thermodynamic trends obtained for the operational range of the O_2/C ratios.

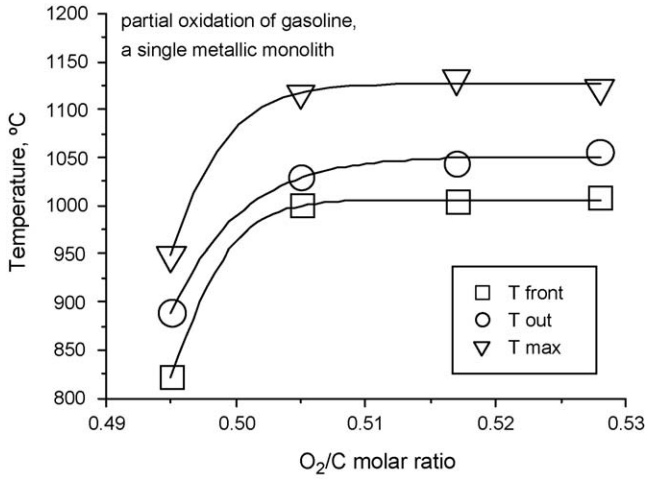

Fig. 4. Effect of O_2/C ratio on the catalyst temperature; gasoline flow rate: 0.893 kg/h.

It should be noted that fuel-oxygen ratio is the most important tunable parameter for the reformation of the high energy density gasoline fuel. Only two percent altering in the air flow rate at the same feeding of gasoline causes a pronounced impact on both the adiabatic temperature and reformate composition (see also Ref. [34]). According the experimental observations, enhancing exothermicity of the gasoline partial oxidation reaction by increasing O_2/C molar ratio in the feed causes an increase in the outlet temperature while the front-face temperature changes only slightly (Fig. 6, left). Comparing to the ceramic monolith, thermal axial (longitudinal) gradient is minimized in the metallic monoliths. A similar trend was observed for the radial (transversal) catalyst temperature. Maximum difference of 60 °C was detected between the axial and wall temperatures in the reactor with the metallic monolith against the difference of 90 °C for microchannel cermet catalyst [34]. Therefore, the catalyst-bed with high conducting properties may act as a heat exchanger through the proper axial distribution of the process heat. For the two metallic monoliths bed of such configuration, an oxygen-to-carbon ratio in the feed affects the axial temperature profile through the reactor rather than the feed flow rate (Fig. 6, right).

Thus, the metallic monolithic catalysts developed at Boreskov Institute of Catalysis may secure an extremely efficient dissipation of reaction heat through a proper choice of support material and monolith geometry.

3.1.2. Autothermal radial-flow reactor

Table 1 and Fig. 7 show the results of testing the autothermal radial-flow reactor in the partial oxidation of natural gas (94% CH_4, 3% C_2H_6, 2% C_3H_8, 0.4% C_4H_{10}, 0.1% CO_2 and 0.5% N_2) with air. The autothermal radial-flow reactor demonstrated stable performance at the variation of flow rate from 4.3 to 14.4 m^3/h. The data in Table 1 suggest that, as expected, the general behavior of the methane partial oxidation process in terms of the temperature in the multiple catalyst-beds cylindrical architecture was similar to that observed for the axial flow monolith reactor. Temperature

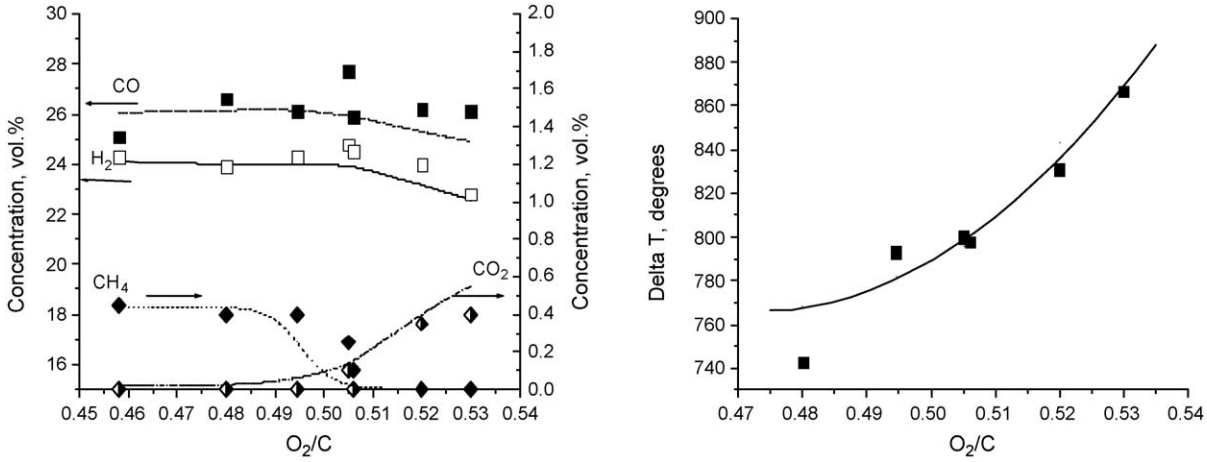

Fig. 5. Gasoline partial oxidation by air over two metallic monoliths. Experimentally measured values (symbols) and thermodynamic predictions (curves) for the product gas (left) and adiabatic temperature rise (right) in the partial oxidation of gasoline versus O_2/C molar ratio in the feed stream. The feed temperature of 190–210 °C.

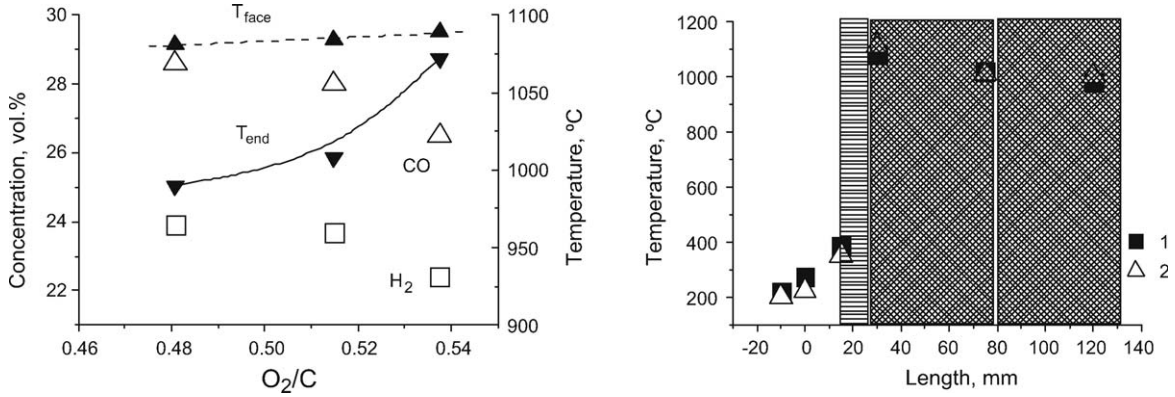

Fig. 6. Gasoline partial oxidation by air over two metallic monoliths. Left: effect of air-fuel ratio (expressed by O_2/C mole ratio in the feed) on hydrogen and CO concentration (open symbols) in syngas and the temperature (filled symbols). Gasoline flow rate: 0.893 kg/h. Right: the temperature profiles along the reactor axis at the steady state and O_2/C = 0.48. Mode 1: 0.893 kg/h gasoline, 3.31 m^3/h air (STP) (O_2/C = 0.48), U_o = 0.42 m/s and 0.19 s contact time, T_{in} = 220 °C; mode 2: 1.86 kg/h gasoline, 6.90 m^3/h, U_o = 0.9 m/s and 0.09 s contact time, T_{in} = 206 °C.

reaches the highest value at the very front of the radial-flow monolith consisting of the washers. The temperature profile across the radial-flow reactor catalyst-beds declines towards the exit of the reactor. We think it is important that the radial-flow arrangement shows a high stability in the temperature in both the radial-flow monolith and gauze catalyst-bed at the feed volume flow rate being variated. Conversion of natural gas and selectivity to syngas in the partial oxidation process remain also stable and almost independent of the flow rate (Fig. 7) due to the high conducting properties of the metal catalysts and minimization of heat loss.

The reversible nature of these reactions imposes a limit, determined by thermodynamic equilibria, on the conversion and yields of CO and H_2. Thermodynamic equilibrium compositions (on the dry basis, same as that measured by the GC) under the experimental conditions at the reactor exit temperature (tagged as footnote 'a' in Table 1) and the gauze bed temperature (tagged as footnote 'b') suggest that CO and H_2 concentrations in the product gas are most likely determined by equilibria at the temperature in the microspheroidal catalyst-bed at a position close to the gauze bed. Unfortunately, no data available from this zone of the radial-flow reactor.

Table 1
Autothermal radial-flow performance results. Feed: natural gas-air mixture with O_2-to-CH_4 = 0.768.

Flow rate, m^3/h (STD)	Superficial velocity, m/s (STD)	Temperature, °C[a]				Product species (experiment/thermodynamics), v/v%			
		Feed inlet	Radial-flow monolith inlet	Gauze bed outlet	Exit	H_2	CO	CO_2	CH_4
4.3	0.16	486	1146	832	648	**30.1**/[a]27.4/[b]32.6	**14.3**/[a]12.1/[b]17.0	**3.74**/[a]5.0/[b]2.1	**3.85**/[a]3.7/[b]0.1
8.9	0.34	473	1179	877	757	**31.4**/[a]32.1/[b]32.6	**15.7**/[a]16.2/[b]17.3	**3.35**/[a]2.7/[a]1.9	**2.92**/[a]0.5/[b]0.04
9.3	0.35	467	1111	868	737	**31.8**/[a]31.7[b]32.6	**16.6**/[a]15.8/[b]17.2	**3.23**/[a]2.9/[b]2.0	**2.03**/[a]0.8/[b]0.06
14.4	0.54	386	1014	854	503	**31.2**/[a]14.1/[b]32.6	**16.1**/[a]2.8/[b]17.2	**3.75**/[a]10.5/[b]2.0	**3.56**/[a]11.7/[b]0.06

Notes: positions of the thermocouples are shown in Fig. 2. Bold values for measured concentrations.
[a] Equilibrium at the exit temperature.
[b] Equilibrium at the outlet temperature of the gauze bed.

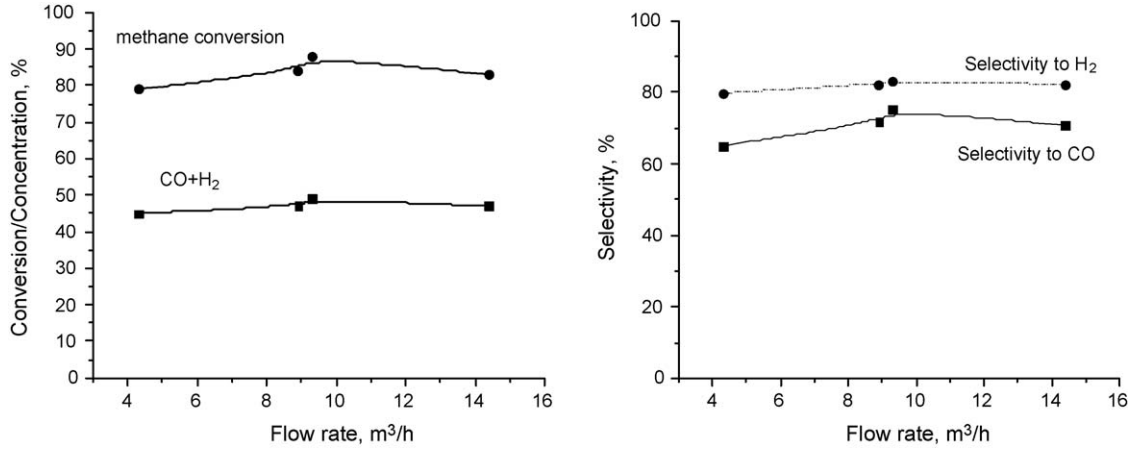

Fig. 7. Partial oxidation of natural gas in the autothermal radial-flow reactor. Methane conversion and syngas concentration (left), and selectivity versus flow rate (right).

The most prominent deviation from the measured concentrations (bold values in Table 1) appeared in the thermodynamic predictions calculated at the reactor exit temperature for the case of 14.4 m^3/h flow rate. The exit temperature is rather low in this case due to a high heat release in the recuperative heat exchange between the cold feed stream and hot product gas. However, the syngas yield is of a high value. Seemingly, direct quenching of the product gas occurs by the cooling in the microspheroidal catalyst-bed through the heat exchange with reacting gas. Indeed, due to the cooling of the reactants, a higher conversion becomes possible; simultaneously the new arrangement is more energy efficient by providing the energy needed for preheating the feed.

3.2. The thermodynamics calculations

It is known that at full conversion of hydrocarbons, irrespective of whether a thermal or catalytic technology or fixed or fluidized catalyst-bed is used, the composition of the product exit gas will be determined by thermodynamic equilibrium corresponding to the outlet temperature of the catalytic bed, which is dictated by the inlet temperature, the feed composition, and the reaction heat evolved (adiabatic temperature rise). Obviously, this is only the case if all necessary reactions can take place because the proper catalyst is used, and the residence times in the catalyst-bed are long enough [19]. Nowadays, thermodynamic theory is even considered to be enabling to derive mass-action kinetics [52,53]. Therefore this question is of high practical relevance.

A calculation of chemical equilibrium for the composition is one of two levels of sophistication in treating the chemistry. By using thermodynamic study, a better correlation can be established between product composition, temperature, overall energy conversion efficiency, and different operating conditions such as feed composition. Generally, the thermodynamic equilibrium in a reformer reactor depends on the following parameters:

- preheat temperatures of the reactor feed (air, water, and fuel)
- pressure inside the reactor
- chemical composition of the fuel
- heat loss
- fuel-to-air and/or -water ratios.

If these parameters are given, the thermodynamic equilibrium of the system can be calculated by means of minimizing the Gibbs energy. The equilibrium computations provide a more realistic estimate of the expected product composition and thermal efficiency of the process. Fuel/air/steam ratio in the feed is a primary parameter which determines both hydrogen yield in the product gas (reformate) and the energy released or absorbed by the reaction and hence, the adiabatic reaction temperature.

Specification of the system components (not the reactions) was used in the thermodynamic consideration. The equilibrium model was based on the following simplifications: uniform temperature and pressure are assumed; no information about actual reaction pathways/formation of intermediates; no tar, no solid carbon are modeled; no information about the rate of the reactions. In addition to the reacting system (a mixture of air and organic compounds as methane, isooctane and surrogate gasoline), such components as H_2, CO, CO_2, H_2O, CH_4, C_2H_2, C_2H_4, C_2H_6, C_3H_6 and C_3H_8 were taken into account to determine the resultant mixture composition as a function of oxygen-to-carbon ratio, steam-to-carbon ratio, temperature, pressure, and product species. The Peng–Robinson equations of state were used to calculate the stream properties. The HYSYS software package (HyproTech. HYSYS.Process.v2.2 AEA Technology) has been used in the parametric study.

A correct representation of the thermochemical properties of hydrocarbon fuel is very important for providing a more realistic estimate of the expected parameters. This requires identification of the possible components. However, liquid fuel is a complex mixture of hydrocarbons. Gasoline fuel is a mixture of normal paraffins, isoparaffins, cycloalkanes, aromatics and olefins. In our case, the tested gasoline contained 191 types of hydrocarbons. The amount of aromatics was about 40 wt.%. According to the chromatographic analysis data, a generic formula for the averaged composition corresponds to $C_{7.2}H_{13.36}$. Thus, a model fuel is required which is sufficiently flexible to incorporate a large number of compounds/interactions and provide good results [6,7,54–57]. The surrogate gasoline mixture that was specified for modeling was an equilibrium distribution of the 29 close-cut fractions C_3–C_{10} identified according to the following three criteria: sum of carbon and hydrogen atoms identical to that of gasoline; closely matching fractional distillation diagrams; and low heating value [35,36]. The characteristics of the fuels, both of the base gasoline employed in the experimental study and the surrogate used as a model in the thermodynamic calculations, are summarized in Table 2. As anticipated, the two types of fuels display good similarity. Available data from the experimental observations confirm the reliability of such approach: both the product composition and the catalyst outlet temperature are very close to the values thermodynamically predicted by using the model of the base gasoline (Fig. 5).

It is desirable for reformed gas to contain a level of the H_2 concentration as high as possible. Obviously, the concentration of hydrogen in the product gas will depend on the number of

Table 2
Characteristics of the base gasoline and surrogate mixture.

Fuel characteristic	Base gasoline	Model gasoline
C/H ratio	0. 539	0.539
Low heating value, MJ/kg	44.5	43.1
Data of fractional distillation, °C:		
Start point	42	38
10 wt. %	73	71
50 wt. %	112	110
90 wt. %	165	170
End	185	182
Density, g/ml (20 °C)	0.78	0.8

hydrogen atoms per carbon in the fuel. The maximum achievable concentration of hydrogen for the considered fuels decreases in the order: methane (41%) > isooctane (28.1%) > gasoline (24.3%), according to the reaction stoichiometry. The actual product composition and efficiency of the reforming process are dependent on reactivity of the specific fuel and their components also. It is clear that the fuel reforming efficiency to synthesis gas is directly proportional to the amount of hydrogen and carbon monoxide generated and reaches its maximum at the minimum value of the air ratio and its minimum at the maximum of the air-to-fuel ratio [54]. The most important reactor parameters are supposed to be the reaction temperature and gas flow rate considered generally in terms of the residence time in the reactor [58–60]. The syngas formation efficiency is also coupled to the feed temperature. Let us apply thermodynamics consideration to give a systematic discussion of how the reaction parameters affect the performance of syngas formation from methane, isooctane and gasoline.

Effect of the reaction temperature. Fig. 8 shows the product distribution in the reformed gas versus reaction temperature for the given O_2/C molar ratio in the given feed. It can be seen that for all hydrocarbon fuels considered in the calculations the conversion does not require too high temperature. In a practical temperature range of 800–1200 °C for the partial oxidation reforming reaction occurring at 1 atm, concentrations of hydrogen and carbon monoxide in the product gas change only weakly. The point is to discover an optimal value of the reaction temperature required, e.g., to reduce the carbon deposition and methane formation which are thermodynamically favored at lower temperatures. From the thermodynamic point of view [54], the formation of solid carbon (soot or coke) mainly depends on the ratio of carbon to hydrogen in the fuel, as well as on the air to fuel ratio and steam to carbon ratio. Yet, the higher operational temperatures would tend to form by-products (e.g. olefins, cyclic products) during partial oxidation/reforming.

Effect of pressure. From Le Chatelier's principle it is clear that oxidation equilibria are also favored by the low pressure. Increase of pressure has a negative effect on both the hydrogen yield and the operational temperature (see Figs. 9 and 10). For the gasoline partial oxidation the lower limit of about 750 °C could be determined at 1 atm, while the pressure of 15 atm results in the operational temperature of about 1000 °C.

Effect of the feed preheating temperature. Obviously, the higher preheat temperature results in the lower reforming efficiency. Effect of the feed temperature on the reaction temperature in adiabatic reactor and syngas formation may be clarified by the thermodynamic considerations shown in Fig. 11 and experimental data illustrated in Figs. 12 and 13.

At designing a fuel preheating system including the fuel-air mixture preparation with fuel atomization and vaporization, one should take into account the fuel reactivity towards thermal cracking and pre-reforming reactions in the gas feed. Although methane is the most abundant of alkanes, it is also the least

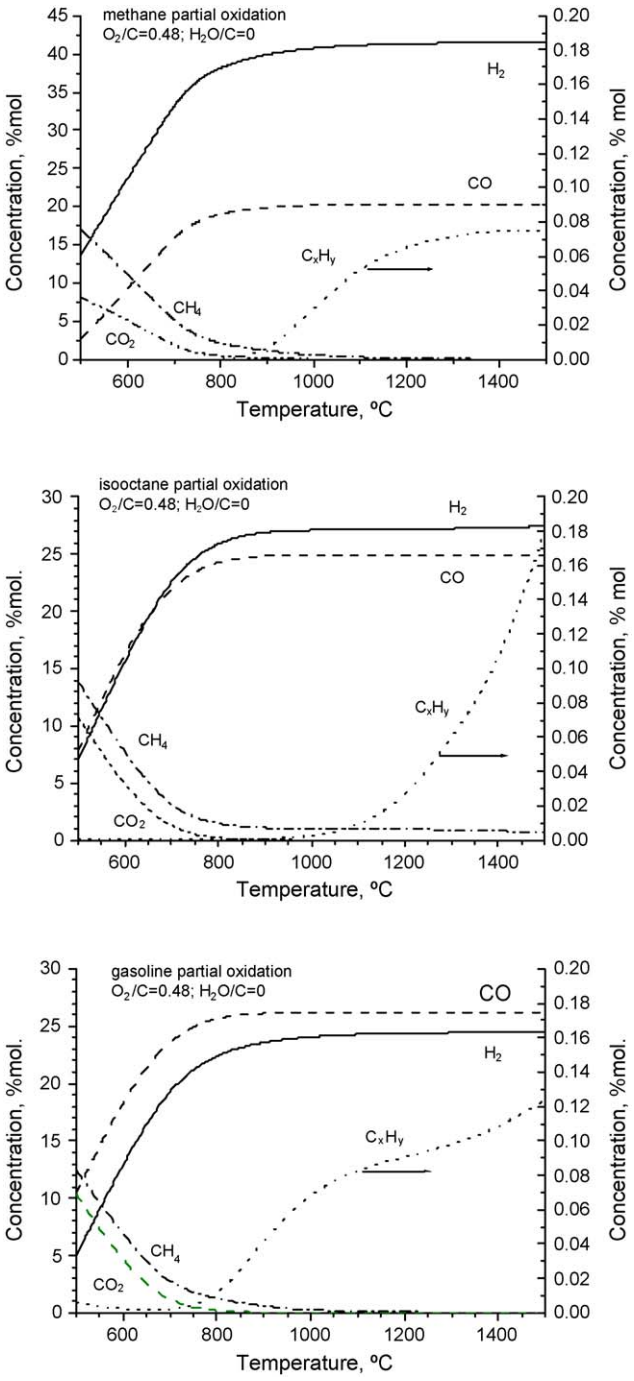

Fig. 8. Thermodynamic predictions of equilibrium gas composition produced in the isothermal partial oxidation of methane, isooctane and gasoline with air as a function of temperature. P = 1 atm.

reactive [61]. We found that the experimental data collected over honeycomb corundum catalysts (Fig. 12) were consistent with the stated thermodynamic predictions for the methane partial oxidation also. The preheat temperature of the methane–air mixture can exert an important effect on the choice of the operational O_2/C ratio (see Fig. 10), the reaction temperature, and syngas formation (Fig. 11). However, isooctane and even more so gasoline fuels are much more reactive towards cracking compared to methane, especially in the mixture with air.

According to direct experimental observations in the isooctane partial oxidation, the catalyst temperature tends to decrease with preheating of the isooctane-air mixture (Fig. 13, left). The fractional

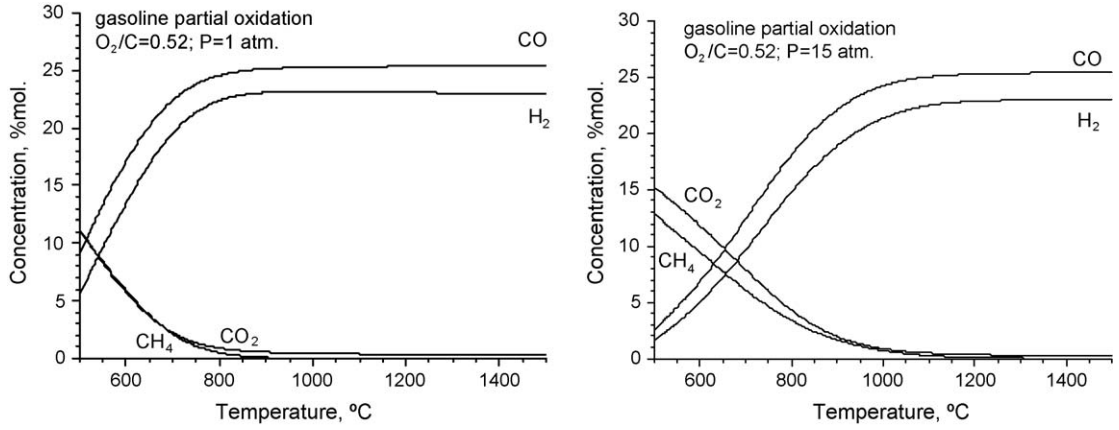

Fig. 9. Effects of the temperature and pressure on main products in the equilibrium reformate gas at the isothermal partial oxidation of gasoline with air.

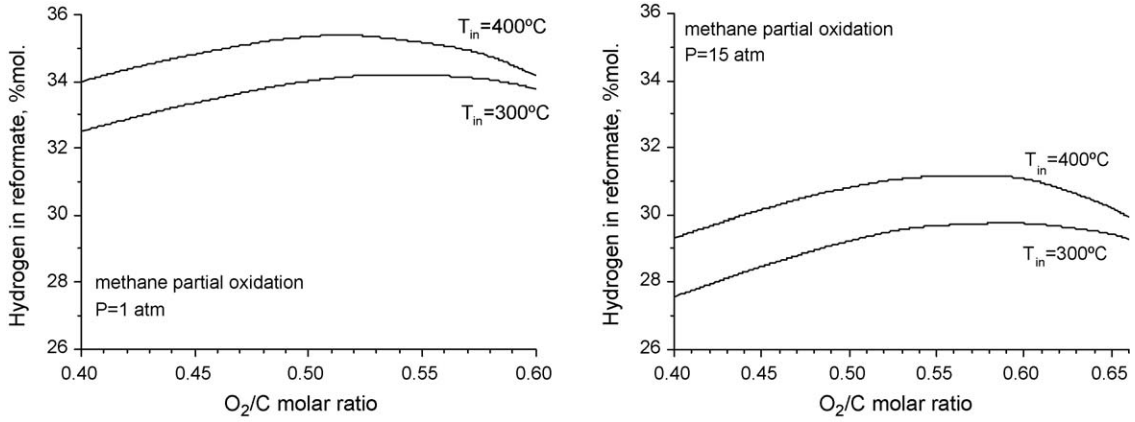

Fig. 10. Effect of the O_2/C ratio in the methane–air feed with the different preheat temperature on the hydrogen concentration in the product gas (adiabatic reactor). Thermodynamic predictions for P = 1 atm (left) and P = 15 atm (right).

composition of gasoline was observed to be altered even at 200 °C preheat of the feed [35,36]. In the gasoline partial oxidation, the catalyst temperature is just slightly increased with an increase in the temperature of gasoline-air mixture to about 240 °C and then decreased with further preheat due to non-catalytic pre-reforming reactions (Fig. 13, right). In point of fact, the preheat temperature of about 190 °C was found to be the preferable one for the gasoline-air feed.

Effect of the O_2/C molar ratio in the feed on the level of hydrogen in the product gas and the reaction temperature is found to be

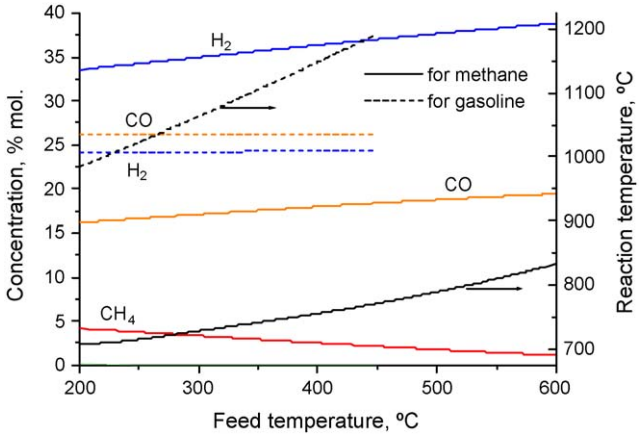

Fig. 11. Thermodynamic predictions on the effect of the feed temperature in the partial oxidation of methane and gasoline by air at adiabatic conditions. O_2/C = 0.50, P = 1.0 bar.

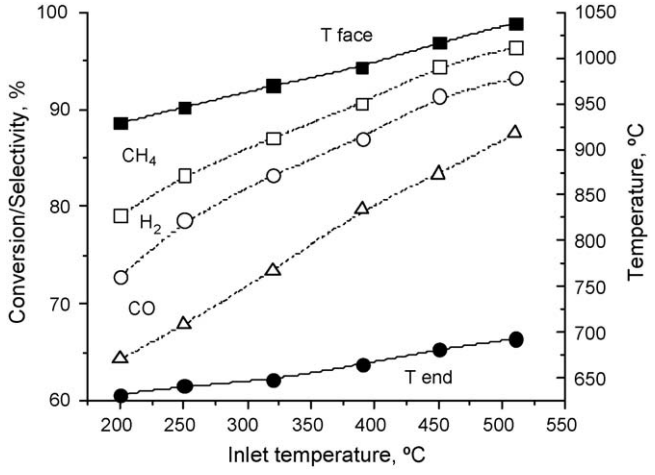

Fig. 12. Experimental data on the effect of inlet temperature on the process performance over corundum monolith (0.2 wt.% Pt/7 wt.% LaNiO) with triangular shape channels (d_{eq} = 0.67 mm, ε = 0.6): 27 v/v% CH_4 in air, U_o = 0.4 m/s, 0.15 s (STP) contact time.

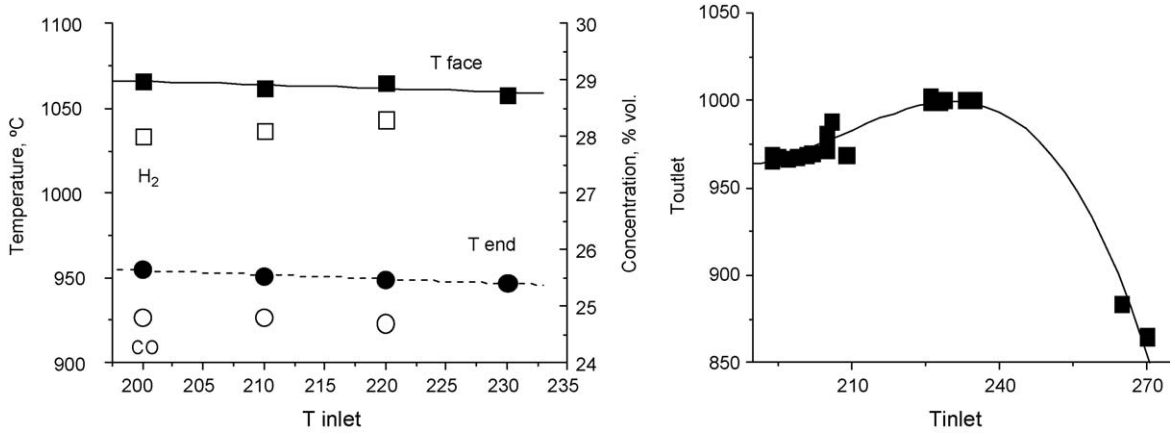

Fig. 13. Effect of the inlet temperature on the partial oxidation process performance over metallic catalyst. Left: isooctane 0.757 kg/h in air, O_2/C = 0.53, 0.1 s (STP) contact time; right: gasoline 0.894 kg/h in air, O_2/C = 0.53, 0.1 s (STP) contact time

much more pronounced for gasoline reforming than those for methane and even for isooctane (Fig. 14). Optimal processing of gasoline occurs in the restricted range of O_2/C = 0.50–0.52 in which the concentrations of hydrogen in the product gas correspond to the calculated values of 24.08–23.15 mol%, respectively (dry gas). For the fixed input temperature (200 °C), thermodynamic calculations show that with variation in the O_2/C molar ratio from 0.5 to 0.52 in the feed the adiabatic temperature rise increased from 787 to 840 degrees. Further increasing the O_2/C molar ratio may cause deactivation of the catalyst due to the high temperature in the frontal part of the monolith, as it was observed in Ref. [34]. Compared to gasoline, the moderate heat evolved and smaller increase in the temperature (about 40 °C) is observed for isooctane in the same range of the O_2/C ratio. This enables operating at the higher values of O_2/C ratios in the isooctane-air mixture. A much more weak dependence on the O_2/C ratio is observed for methane partial oxidation. In this case, it is desirable not only to preheat the feed mixture to a high temperature, but operate at O_2/C ratio of about 0.6, which is higher than the stoichiometric one (see also Ref. [62]).

It was demonstrated in our experiments [35] that the predictions for the equilibrium composition at the monolith back face temperature in the autothermal reforming mode (with steam addition) are in very good agreement with the experimental data as well. Effects of such parameters of the feed gas as the steam and oxygen-to-carbon ratios on the autothermal reforming of gasoline are highlighted with Fig. 15. It is important to feed sufficient oxygen, so the energy generated by the oxidation compensates the energy absorbed by the endothermic reactions.

Well defined maximum in the hydrogen concentration in dry reformate is observed at the H_2O/C molar ratio of about 1.0 in the considered range of the O_2/C ratio in the feed (Fig. 15, left). This value will correspond to the maximum reformer efficiency, because further increasing in the hydrogen yield would require an additional energy input to dry the reformate gas. To keep the reaction temperature at about 800 °C for the given input temperature of 270 °C and steam-to carbon ratio of about 1.0, the oxygen-to-carbon ratio needs to be maintained at the value of about 0.45. At these operational parameters the thermodynamic calculations predict the hydrogen concentration in the product gas of about 29 mol%.

The thermodynamic analysis allows one to outline only a range of favorable operational conditions that is required for the product distribution and conversion efficiency of hydrocarbon fuels in a reforming reactor. Generally, for a practical consideration, the operational characteristics should be chosen on the base of analysis of many factors including a range of throughputs, design of the reactor and configuration of monoliths, as well as catalytic activity. A complementary approach is kinetic description of chemically reacting system.

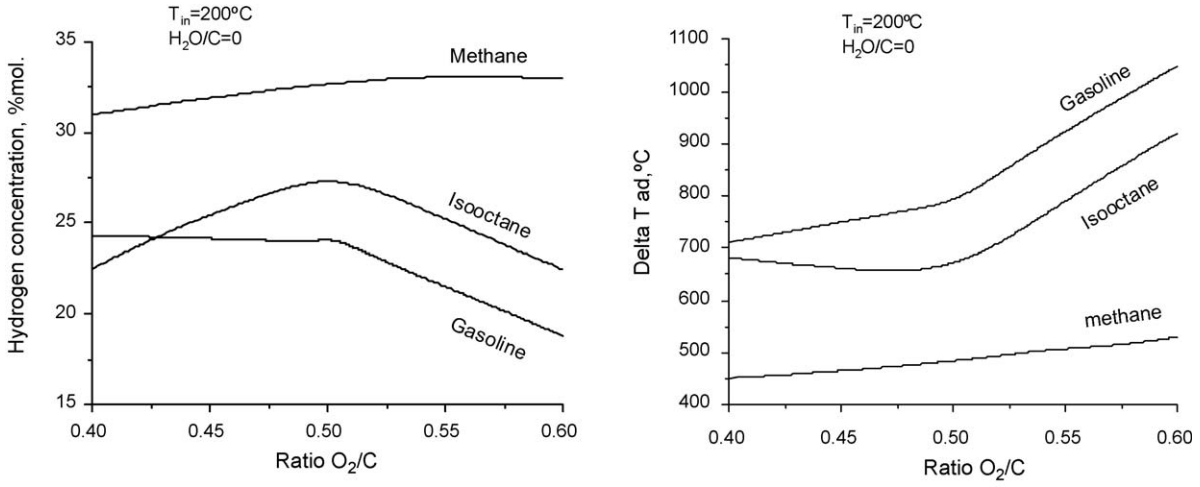

Fig. 14. Effect of the molar oxygen-to-carbon ratio in the fuel–air mixture on the hydrogen concentration and adiabatic temperature rise at the partial oxidation of methane, isooctane and gasoline with air.

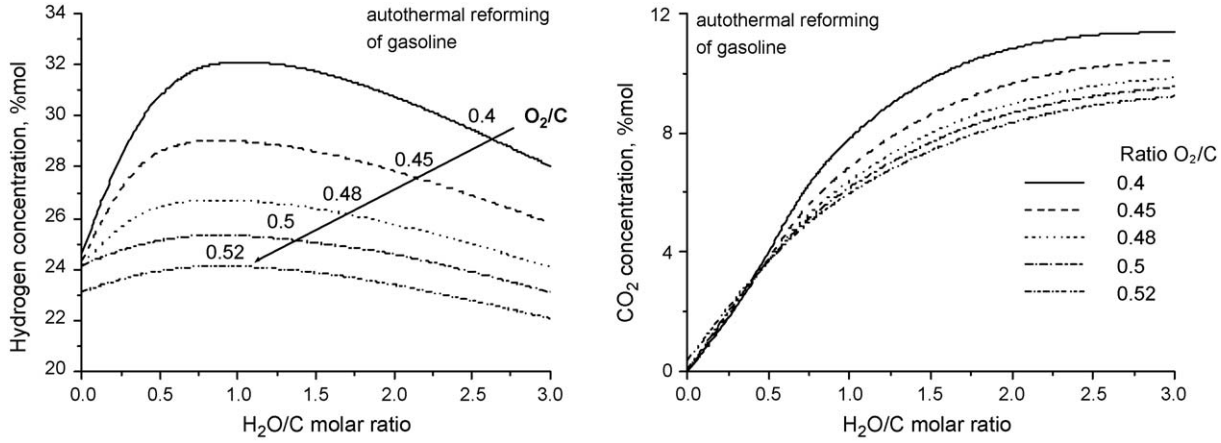

Fig. 15. Effect of the H_2/C and O_2/C molar ratios on the content of H_2 and CO_2 in the product dry gas in autothermal reforming of gasoline. Feed temperature T_{in} = 270 °C.

3.3. Numerical study of the partial oxidation of methane

By using the thermodynamic calculations we can establish a correlation between the inlet and outlet characteristics of an adiabatic reactor at steady state. The catalytic reactors used for the oxidative conversion of hydrocarbon fuels to syngas and loaded with catalysts of different forms such as foam or extruded monoliths, wire gauzes, or sintered spheres, have a complex interaction between the reactive flow and reactions on the catalytic surface. A significant amount of the chemistry in this system takes place in the entrance region of the catalyst. These catalytic processes, which can be run nearly autothermally and adiabatically, exhibit an extremely fast variation of temperature, velocity, and transport coefficients of the reactive mixture near the catalyst entrance [63,64]. Spatio-temporal profiles developed in the monolithic catalyst are results of interplay among kinetics, hydrodynamics, and heat transfer. The physical-chemical processes in the monolith reactor may be examined in detail by the mathematical simulation studies.

The basic reactor and methane partial oxidation reaction model for the Pt/Ce–Zr–La/α-Al_2O_3 honeycomb monolith has been presented in detail in a separate paper [65]. A dynamic one-dimensional two-phase reactor model of the processes with accounting for both transport limitations in the boundary layer of a fluid near the catalyst surface and detailed molecular unsteady-state kinetic model for surface reactions has been developed and verified with the transient experiments data. A mechanism proposed by Aghalayam et al. [66] was taken as a basis for the unsteady-state kinetic model to be implemented in the dynamic reactor model after some modification. The Pt/Ce–Zr–(La)/α-Al_2O_3 honeycomb monolith is a complex catalytic system where washcoat (fluorite-like nano-crystallites of solid solution CeZr/CeZrLa) closely interacts with active component Pt. Study of detailed kinetic and mechanism of the partial oxidation reaction using the step response technique has made it clear that active oxygen of the bulk quickly re-oxidizes the reduced platinum [25]. The simplified reaction scheme illustrates the reaction mechanism over the Pt/CeO_2–ZrO_2 catalyst:

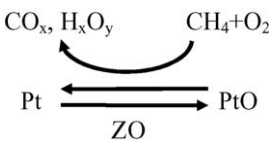

The unsteady state kinetic model of the partial oxidation of methane over the catalyst accounts for the interaction of washcoat (Z, ZO) with active catalyst sites (Pt, PtO) (reaction 32 in Table 3). The implemented detailed mechanism contains 32 elementary steps of methane oxidation, 14 gaseous compounds and 13 intermediates on the catalyst surface with corresponding kinetic parameters.

The reactor model coupled with the detailed elementary step unsteady-state kinetic model was applied to test the simulation results against available transient experimental data of the reaction ignition during start-up. Due to their high sensitivity to the specific reaction path taken during the transient excursion of the reaction system, good correlations in such comparison approve reliability of an applied mathematical model [64,67].

The experimental data with the full-size hexagonal corundum extruded monoliths with triangular shape channels and active component comprising 0.4% platinum on ceria–zirconia–lanthanum fluorite-like solid solution were taken for comparison with the numerical results. The numerically predicted gas-phase axial temperature profiles as the functions of time (curves) in comparison with the measurements (symbols) are given in Fig. 16.

Generally, the simulation is shown to be in good agreement with the experimental results, yet for the first 20 s the predicted temperature in the front part of the monolith increases slightly faster than the experimentally measured temperature. During this time the hottest part was found to be at the length of 0.01 m in the experiment and at 0.005 m in the simulations. The error bar of the measurements certainly existed, but the slower temperature rise in the experiments in comparison with the 2D modeling data was also noted by Schwiedernoch et al. [64]. The numerically predicted concentrations of components in the product gas (Fig. 17a) are compared with the experimentally derived data (Fig. 17b). Again, a fair qualitative agreement between the measured and simulated species profiles is observed. During light-off, carbon dioxide, as a product of complete oxidation of methane, appears initially. Then, synthesis gas selectivity slowly increases with rising temperature. On the contrary to the data derived from the experiment with the rhodium coated monolith [64], where CO formation starts before hydrogen formation, hydrogen is detected first during the ignition of Pt/Ce–Zr–La/α-Al_2O_3 monolith. And again, the simulated gas phase composition reaches steady state faster than it was in the transient experiment. This fact was observed again by Schwiedernoch et al. [64]. A special study should be undertaken to clarify the matter discussed. However, the detailed reactor and reaction models can be applied in studying non-stationary/non-equilibrium area to obtain fine details of chemical processes. Detailed simulations allow insights into processes which could not be gained through experiments alone, particularly when extreme reaction conditions (such as very high temperatures) are involved.

Table 3
Surface reaction mechanism for oxidation of methane over Pt/Ce–Zr–La/α-Al_2O_3.

No.	Reaction	k_f preexponential, s^{-1} or sticking coefficient	E_f, kcal/mole	k_b preexponential, s^{-1}	E_b, kcal/mole	$\Delta_r H$, kcal/mole
1	$OH^* + * \leftrightarrow H^* + O^*$	5.60×10^{11}	18.3	1.70×10^{10}	13.4	4.9
2	$H_2O^* + * \leftrightarrow H^* + OH^*$	1.20×10^{10}	39.1	3.50×10^{11}	0.0	39.4
3	$H_2O^* + O^* \leftrightarrow 2OH^*$	1.00×10^{11}	34.1	1.00×10^{11}	0.0	34.1
4	$H_2 + 2^* \leftrightarrow 2H^*$	0.09	0.0	3.33×10^{12}	20.0	−16.0
5	$O_2 + 2^* \leftrightarrow 2O^*$	0.03	0.0	1.00×10^{11}	19.0	−15.0
6	$H_2O + * \leftrightarrow H_2O^*$	1.00	0.0	5.33×10^{12}	10.0	−10.0
7	$OH + * \leftrightarrow OH^*$	1.00	0.0	1.00×10^{13}	30.0	−30.0
8	$H + * \leftrightarrow H^*$	1.00	0.0	1.00×10^{13}	60.2	−60.2
9	$O + * \leftrightarrow O^*$	1.00	0.0	1.00×10^{13}	67.0	−67.0
10	$CH_4 + 2^* \leftrightarrow CH_3^* + H^*$	0.68	12.0	3.97×10^{10}	5.5	6.5
11	$CH_3^* + * \leftrightarrow CH_2^* + H^*$	1.32×10^{13}	25.8	4.04×10^{10}	6.1	19.7
12	$CH_2^* + * \leftrightarrow CH^* + H^*$	1.00×10^{11}	25.0	1.00×10^{11}	12.2	12.8
13	$CH^* + * \leftrightarrow C^* + H^*$	1.00×10^{11}	5.4	1.00×10^{11}	37.6	−31.4
14	$CH_3^* + O^* \leftrightarrow CH_2^* + OH^*$	1.00×10^{11}	17.7	1.00×10^{11}	3.1	14.6
15	$CH^* + OH^* \leftrightarrow CH_2^* + O^*$	1.00×10^{11}	13.2	1.00×10^{11}	20.5	−7.3
16	$C^* + OH^* \leftrightarrow CH^* + O^*$	1.00×10^{11}	38.2	1.00×10^{11}	1.5	36.7
17	$CH_2^* + H_2O^* \leftrightarrow CH_3^* + OH^*$	1.00×10^{11}	19.5	1.00×10^{11}	0.0	19.5
18	$CH^* + H_2O^* \leftrightarrow CH_2^* + OH^*$	1.00×10^{11}	26.7	1.00×10^{11}	0.0	26.7
19	$C^* + H_2O^* \leftrightarrow CH^* + OH^*$	1.00×10^{11}	70.9	1.00×10^{11}	0.0	70.9
20	$CO^* + * \leftrightarrow C^* + O^*$	1.00×10^{11}	74.2	1.00×10^{11}	0.0	75.
21	$CO_2^* + * \leftrightarrow CO^* + O^*$	1.00×10^{11}	43.1	1.00×10^{11}	0.0	43.1
22	$CO + * \leftrightarrow CO^*$	0.71	0.0	1.21×10^{13}	34.0	−34.0
23	$CO_2 + * \leftrightarrow CO_2^*$	0.7	0.0	1.46×10^{12}	17.0	−17.0
24	$CO_2^* + H^* \leftrightarrow CO^* + OH^*$	1.00×10^{11}	38.2	1.00×10^{11}	0.0	38.2
25	$CO^* + H^* \leftrightarrow CO^* + O^*$	1.00×10^{11}	106.0	1.00×10^{11}	0.0	106.0
26	$CO^* + H^* \leftrightarrow C^* + OH^*$	1.00×10^{11}	69.2	1.00×10^{11}	0.0	69.2
27	$CH_3 + * \leftrightarrow CO_3^*$	1.00	0.0	1.00×10^{13}	38.0	−38.0
28	$CH_2 + * \leftrightarrow CO_2^*$	1.00	0.0	1.00×10^{13}	68.0	−68.0
29	$CH + * \leftrightarrow CH^*$	1.00	0.0	1.00×10^{13}	97.0	−97.0
30	$C + * \leftrightarrow C^*$	1.00	0.0	1.00×10^{13}	150.0	−149.0
31	$2CO^* \leftrightarrow C^* + CO_2^*$	2.40×10^{12}	31.0	4.17×10^{9}	0.0	31.9
32	$O^* + Z \leftrightarrow * + ZO$	0.2×10^{3}	1.4	0.2×10^{3}	1.4	0.0

The site densities were assumed: for the Pt: 1.65×10^{-5} mol/m^2, for ZO: 1.65×10^{-2}.

Thus, the simulation of the thermal behavior of the foam ceramometal monolith structure (Fig. 18) shows the transient development of the gas temperature (left) and the solid temperature (right) profiles during the light-off process occurred on a time scale of seconds. Large difference between the gas and solid phase temperatures is observed. IR thermography and thermocouple measurements performed by Basini et al. [68,69] have shown large temperature gradients between surfaces and gaseous phases and even higher than estimated adiabatic gas temperatures.

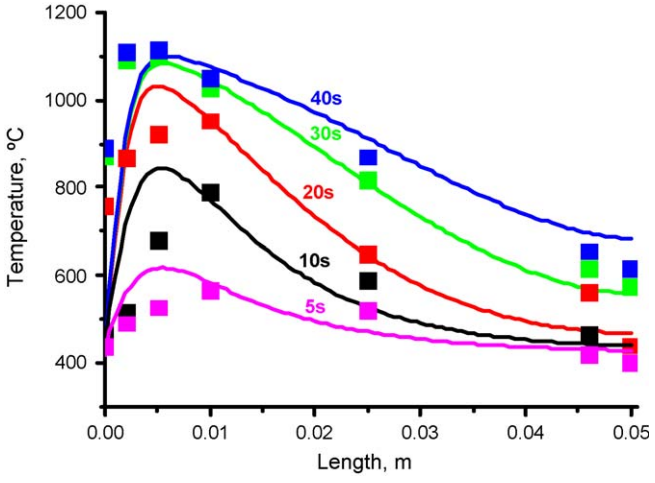

Fig. 16. Gas temperature evolution in extruded monoliths with triangular shape channels during start-up. Feed mixture: 0.24 mol.fr. of CH_4 in air, $T = 420$ °C, $P = 1$ atm, $u = 0.5$ m/s (STP). Lines: modeling predictions; symbols: experimental data.

Complex dynamic behavior of the surface species is revealed by the simulation data. In spite of the fact that the reactants' residence time in the operational conditions is of the order of milliseconds, the vacancies coverage reaches steady state rather slowly (Fig. 19, left) due to the multi-step heterogeneous reaction mechanism. Calculated molar gas-phase concentrations at steady state of methane oxidation in the monolith (Fig. 19, right) show that the main chemical transformations occurred within 10% of length behind the monolith entrance.

Besides the fact that the high surface temperature is a major threat to the stability of supported noble metal catalyst, it is possible that the catalyst generates the radicals, prosecution of the reaction by radical fragments can occur either on the surface or in proximity of the surface in the film at the gas–solid interface or even in the gas phase [10,70]. It is generally believed that at the atmospheric pressure homogeneous reaction paths play a minor role in the methane partial oxidation. To estimate the occurrence of gas phase chemistry at the operational conditions typical for the methane partial oxidation, we apply the detailed kinetic model (see Table 4) based on a free radical mechanism [71] in the reactor model [65]. The gas-phase mechanism contains 40 reversible elementary free-radical reactions with 13 molecules and 10 radicals. General features of the reaction mechanism do not depend on the total pressure. Effect of pressure was taken into account by the variation of the kinetic parameters of the unimolecular reactions. The curve of the pseudo-first order rate coefficient k_u for a unimolecular reaction $A + M \rightarrow A_1 + A_2 + M$ with $r = k_u C_A$, against pressure is called the fall-off curve of the unimolecular reaction. The value of a collision partner M for species A, known as the third-body concentration C_M ("bath gas"), consists of all the species in the reaction mixture. The third-body concentration C_M is commonly used in spite of the term "pressure" falloff [72]. The value for C_M was taken as the weighed sum of

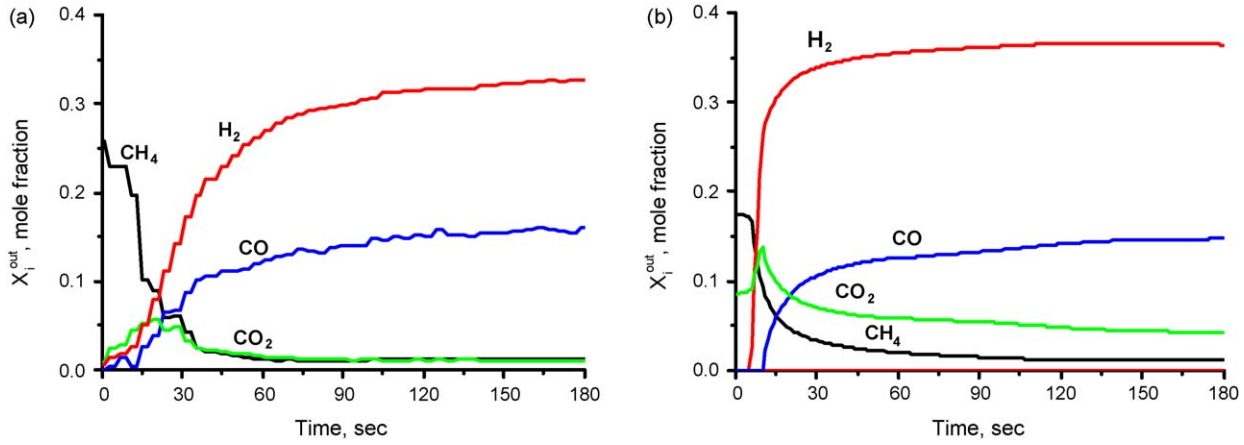

Fig. 17. Time dependencies of main components in the product gas. Feed mixture: 0.267 mol.fr. CH_4 in air, T_o = 400 °C, P = 1 atm, U_o = 0.34 m/s. (a) Experimental data and (b) modeling results.

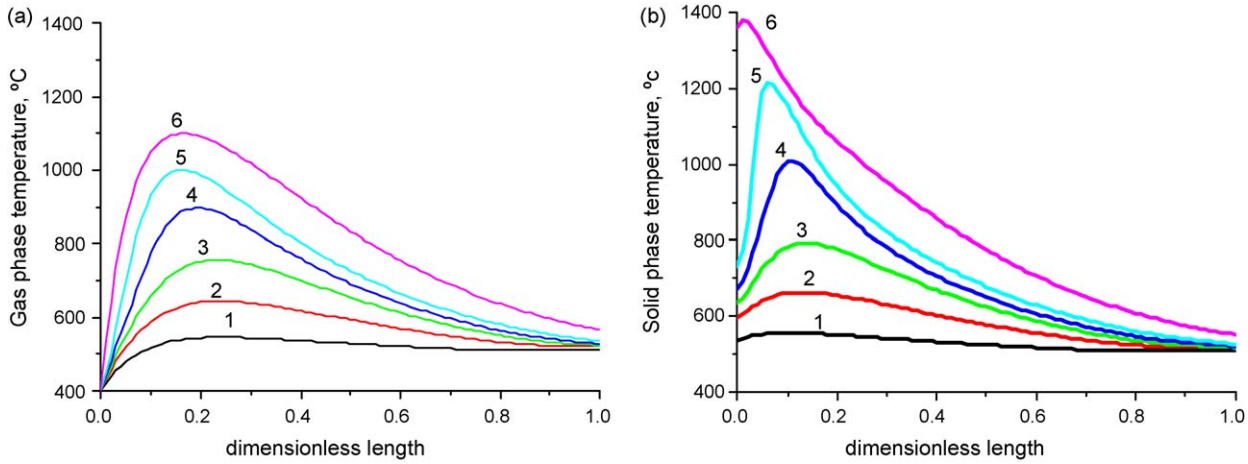

Fig. 18. The temperature evolution in ceramometal monolith (30 PPI) during light-off—(1) in 0.8 s, (2) 2.4 s, (3) 4 s, (4) 5.6 s, (5) 7.2 s and (6) 12 s. Feed mixture: 0.25 mol.fr. CH_4 in air, T_o = 400 °C, P = 1 atm, U_o = 0.5 m/s.

concentrations of all the molecular species. The weight factor w_i takes into account the relative collision efficiencies (assumed to be independent of temperature and reaction) of the third bodies [71]:

$$C_M = \sum w_i C_i$$

The values of the weight factors required for the calculation of the concentration of third bodies were as follows—H_2O: 6.5, CH_4: 6.5, CO_2: 1.5, CO: 0.75, O_2: 0.4 and N_2: 0.4, relative to hydrogen. Other weight factors were equal to unity [72]. The first order approximation is assumed for k_u:

$$k_u = \frac{kC_M}{1 + kC_M} k_\infty,$$

where k_∞ is the rate coefficient for unimolecular reactions at a high-pressure limit. At sufficiently high pressure, that is, when

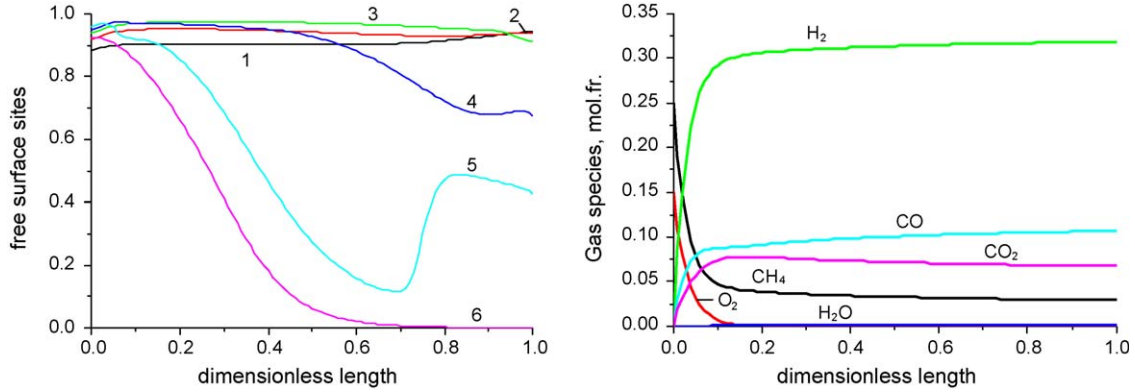

Fig. 19. Free surface sites for the simulated light-off in ceramometal monolith (left): (1) in 0.8 s, (2) 2.4 s, (3) 4 s, (4) 5.6 s, (5) 7.2 s and (6) 12 s, axial distribution of the gas phase species in steady state (right).

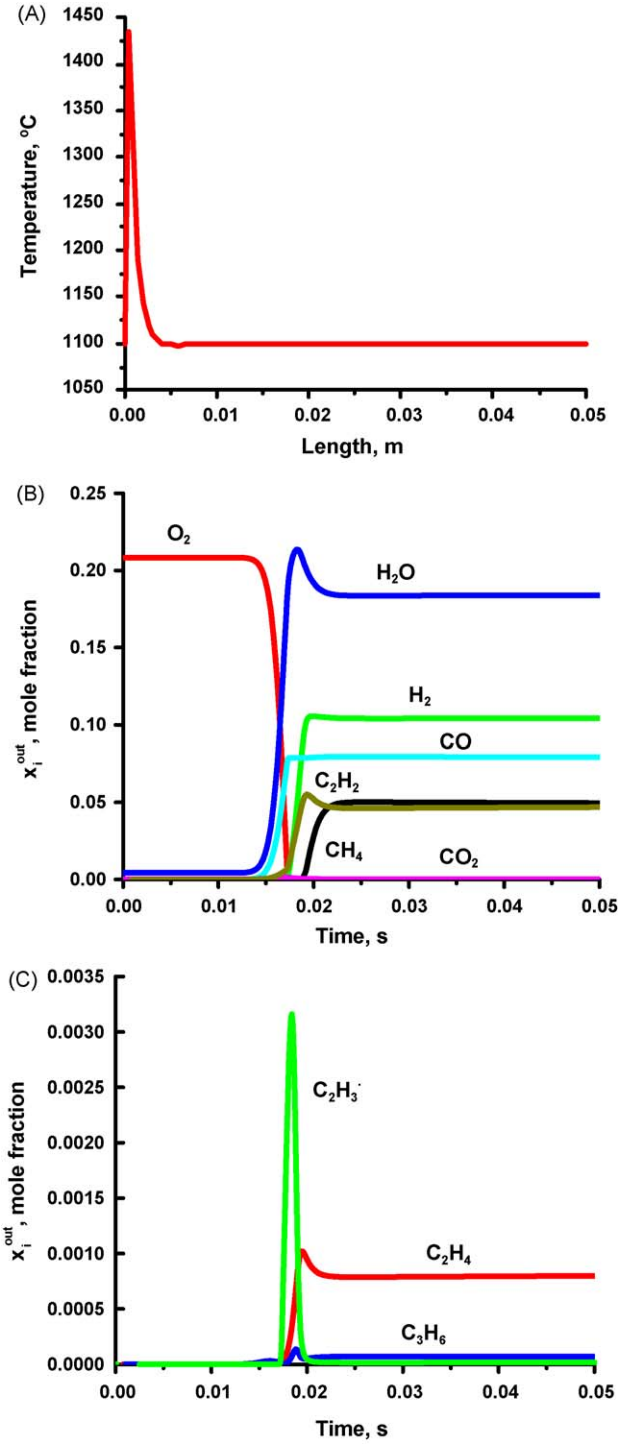

Fig. 20. The simulated gas temperature along a monolith channel in steady state (A) and time dependencies of the main gas species at the exit (B and C). Feed mixture: 0.25 mol.fr. CH_4 in air, P = 1 atm, U_o = 0.7 m/s, T_o = 1100 °C, d_{eq} = 1.15 mm.

$kC_M \gg 1$, k_u is independent of the total pressures and approaches k_∞—the rate coefficient for unimolecular reactions at a high-pressure limit. At low pressure, that is, when $kC_M \ll 1$, k_u becomes proportional to the total pressure, or the total concentration of "third bodies": $k_u = kk_\infty C_M = k_0 C_M$, with $k_0 = kk_\infty$.

The Arrhenius parameters in Table 3 are represented at one of the limiting pressures, either k_∞ (at a high-pressure limit) or k_0 (at a low-pressure limit). For the pressure range of 0.1–2 MPa, the unimolecular reactions 16 and 36 are assumed to be completely in the low-pressure regime. In this case, the pseudo-first order rate coefficient for a unimolecular reaction would be $k_u = k_0 C_M$. The reactions 30, 31, and 33 are assumed to be in the high-pressure regime and are therefore represented in Table 3 without the third body M. The decomposition of $CH_3O^{\bullet}$ (reaction 11) and the decomposition of H_2O_2 (reaction 38) are also mainly in the low-pressure regime, but these are influenced by pressure falloff to some extent at higher pressures:

$$k_u = k_0 \frac{C_M}{1 + C_M \alpha_1 \exp(\alpha_2/(RT))}.$$

Table 4
Model for the gas-phase partial oxidation of methane to synthesis gas in the absence of a catalyst.

No.	Reactions	k_0[a]	E_a, kJ/mol	A/RT
1	$CH_4 + M \rightleftarrows CH_3^\bullet + H^\bullet + M$	0.24×10^{17}	438.98	−6.3
2	$CH_4 + O_2 \rightleftarrows CH_3^\bullet + H_2O^\bullet$	0.398×10^{8}	223.03	0.1
3	$CH_4 + H^\bullet \rightleftarrows CH_3^\bullet + H_2$	0.473×10^{8}	50.31	2.0
4	$CH_4 + O^\bullet \rightleftarrows CH_3^\bullet + OH^\bullet$	0.173×10^{9}	49.12	12.0
5	$CH_4 + OH^\bullet \rightleftarrows CH_3^\bullet + H_2O$	0.659×10^{8}	34.54	4.8
6	$CH_4 + HO_2^\bullet \rightleftarrows CH_3^\bullet + H_2O_2$	0.128×10^{8}	88.18	5.7
7	$CH_3^\bullet + O_2 \rightleftarrows CH_2O + OH^\bullet$	0.396×10^{6}	54.29	37.8
8	$CH_3^\bullet + O_2 \rightleftarrows CH_3O^\bullet + O^\bullet$	0.102×10^{10}	151.30	11.7
9	$CH_3^\bullet + HO_2^\bullet \rightleftarrows CH_3O^\bullet + OH^\bullet$	0.255×10^{8}	0.00	23.6
10	$2CH_3^\bullet + M \rightleftarrows C_2H_6 + M$	0.329×10^{7}	−11.34	6.9
11	$CH_3O^\bullet + M \rightleftarrows CH_2O + H^\bullet + M$	0.383×10^{9}	81.12	7.8
12	$CH_2O + O_2 \rightleftarrows HO_2^\bullet + CHO^\bullet$	0.282×10^{9}	184.27	8.7
13	$CH_2O + OH^\bullet \rightleftarrows CHO^\bullet + H_2O$	0.951×10^{9}	7.74	13.5
14	$CH_2O + HO_2^\bullet \rightleftarrows CHO^\bullet + H_2O_2$	0.461×10^{7}	43.62	14.3
15	$CH_2O + CH_3^\bullet \rightleftarrows CHO^\bullet + CH_4$	0.266×10^{7}	13.39	8.6
16	$CHO^\bullet + M \rightleftarrows CO + H^\bullet + M$	0.835×10^{8}	47.07	3.8
17	$CHO^\bullet + O_2 \rightleftarrows CO + HO_2^\bullet$	0.305×10^{8}	13.74	10.2
18	$CO + HO_2^\bullet \rightleftarrows CO_2 + OH^\bullet$	0.474×10^{8}	73.95	33.5
19	$C_2H_6 + H^\bullet \rightleftarrows C_2H_5^\bullet + H_2$	0.223×10^{9}	44.10	4.5
20	$C_2H_6 + OH^\bullet \rightleftarrows C_2H_5^\bullet + H_2O$	0.230×10^{9}	18.60	7.4
21	$C_2H_6 + CH_3^\bullet \rightleftarrows C_2H_5^\bullet + CH_4$	0.874×10^{9}	97.64	2.5
22	$C_2H_5^\bullet + M \rightleftarrows C_2H_4 + H^\bullet + M$	0.317×10^{15}	195.98	0.8
23	$C_2H_5^\bullet + O_2 \rightleftarrows C_2H_4 + HO_2^\bullet$	0.377×10^{5}	−1.56	7.2
24	$C_2H_4 + H^\bullet \rightleftarrows C_2H_3^\bullet + H_2$	0.542×10^{9}	62.36	4.9
25	$C_2H_4 + OH^\bullet \rightleftarrows C_2H_3^\bullet + H_2O$	0.205×10^{8}	24.86	7.8
26	$C_2H_4 + CH_3^\bullet \rightleftarrows C_2H_3^\bullet + CH_4$	0.416×10^{7}	46.56	2.9
27	$C_2H_3^\bullet + M \rightleftarrows C_2H_2 + H^\bullet + M$	0.200×10^{15}	166.28	0.1
28	$C_2H_3^\bullet + O_2 \rightleftarrows C_2H_2 + HO_2^\bullet$	0.121×10^{6}	0.00	6.5
29	$C_2H_3^\bullet + O_2 \rightleftarrows CH_2O + CHO^\bullet$	0.542×10^{7}	0.00	44.8
30	$C_2H_5^\bullet + CH_3^\bullet \rightleftarrows C_3H_8$	0.105×10^{9}	0.00	3.8
31	$C_2H_4 + CH_3^\bullet \rightleftarrows C_3H_7^\bullet$	0.109×10^{7}	35.64	−0.4
32	$C_3H_8 + H^\bullet \rightleftarrows C_3H_7^\bullet + H_2$	0.238×10^{10}	30.44	4.9
33	$C_3H_7^\bullet \rightleftarrows C_3H_6 + H^\bullet$	0.433×10^{15}	157.69	1.0
34	$C_3H_7^\bullet + O_2 \rightleftarrows C_3H_6 + HO_2^\bullet$	0.119×10^{7}	11.01	7.3
35	$O_2 + H^\bullet \rightleftarrows OH^\bullet + O^\bullet$	0.728×10^{9}	77.91	14.3
36	$O_2 + H^\bullet + M \rightleftarrows HO_2^\bullet + M$	0.150×10^{3}	−6.98	6.4
37	$HO_2^\bullet + HO_2^\bullet \rightleftarrows O_2 + H_2O_2$	0.121×10^{7}	14.92	5.6
38	$H_2O_2 + M \rightleftarrows OH^\bullet + OH^\bullet + M$	0.967×10^{10}	159.66	14.2
39	$OH^\bullet + H_2 \rightleftarrows H_2O + H^\bullet$	0.304×10^{8}	29.08	2.9
40	$HO_2^\bullet + H^\bullet \rightleftarrows OH^\bullet + OH^\bullet$	0.506×10^{9}	3.66	26.2

[a] k_0 is expressed in s^{-1} or $m^3\,mol^{-1}\,s^{-1}$ or $m^6\,mol^{-2}\,s^{-1}$. The relation between the affinity A, the forward ($\vec{r}$) and backward reaction rate ($\vec{r}$) is $\ln(\vec{r}/r\leftarrow) = A/RT$. Conventional two-parametric Arrhenius dependency was used to express the rate constants.

Table 5
Falloff coefficients for the calculations [71].

No.	α_1	α_2	α_3	α_4
1	−0.4904	−2.3380E−03	1.9720E−07	0.75
10	3.9690	−4.8740E−03	3.8020E−07	0.55
22	1.8920	−5.0580E−03	7.2850E−07	0.7
27	0.4197	−2.7810E−03	3.5420E−07	0.75
11	2.3940E−06	2872.3		
38	6.0030E−05	2800.1		

For reactions 1, 10, 22, 27 the falloff data were accurately fitted by correlations:

$$k_u = k_\infty \frac{C_M^{\alpha_4} \exp(\alpha_1 + \alpha_2 T + \alpha_3 T^2)}{1 + C_M^{\alpha_4} \exp(\alpha_1 + \alpha_2 T + \alpha_3 T^2)}.$$

The corresponding falloff coefficients α_i are listed in Table 5.

The calculated with this model temperature along the monolith and time dependencies of main components at the exit are shown in Fig. 20. It has been established that for the typical partial oxidation methane–air mixture and the catalyst operational temperature the local gas phase reactions may occur in the presence of oxygen in gas phase. The calculated concentrations of gas-phase species indicate that the interplay between homogeneous gas phase and catalytic surface reactions may affect considerably the spatial distribution of both the temperature and species at the monolith entrance. High temperatures help to overcome the rather high activation barriers of homogeneous gas-phase reactions with methane, making these reactions 'competitive' with catalytic pathways. For the liquid fuels, which are much more reactive, homogeneous side reactions can change considerably the process selectivities and temperature [34,36], and be even responsible for flames and explosions at high-temperature conditions. Further studies of coupling between catalytic and non-catalytic reactions using a combination of experimental investigations and mathematical simulations are very important from scientific interest and practical point of view.

4. Concluding remarks

In this work we have reviewed some representative results obtained at the Boreskov Institute of Catalysis in the study of high

temperature and high space velocity reactions of synthesis gas formation from hydrocarbon fuels by using both standard and new catalytic reactor configurations. The novel structured catalysts with a low content of noble metals have been developed and tested under conditions which closely approach those of real applications. The integrated reactor concept, in which the heat of the hot reaction products is used to preheat the feed gases internally from the room temperature to ca. 400 °C, was devised for the natural gas partial oxidation. As it was discussed, apart from the heterogeneous reactions, a number of additional chemical and physical phenomena (including the hydrodynamics of the reacting mixture, inter-phase mass and heat transfer, homogeneous reactions) are involved in the reactor performance. The interaction between chemical and physical processes inside adiabatic monolith reactor has been studied by mathematical modeling of the partial oxidation reaction on the base of detailed chemistry. The experimental and simulation data collected and analyzed both in autothermal monolith radial-flow reactors at high space velocity, under the influence of heat and mass-transfer, homogeneous reactions, temperature gradients, provided the key for understanding the reaction nature and interpreting the more complex performance of a millisecond-contact time autothermal reactor in the partial oxidations of methane and liquid fuels.

Acknowledgement

Support by ISTC 2529 Project is gratefully acknowledged.

References

[1] L. Barreto, A. Makihira, K. Riahi, Int. J. Hydrogen Energy 28 (2003) 261.
[2] M.A. Rosen, D.S. Scott, Int. J. Hydrogen Energy 23 (1998) 653.
[3] S. Satyapal, J. Petrovic, C. Read, G. Thomas, G. Ordaz, Catal. Today 120 (3–4) (2007) 246.
[4] D.-J. Liu, T.D. Kaun, H.-K. Hsiu-Kai Liao, S. Ahmed, Int. J. Hydrogen Energy 29 (2004) 1035.
[5] F. Joensen, J.R. Rostrup-Nielsen, J. Power Sources 105 (2002) 195.
[6] M. Krumpelt, T.R. Krause, J.D. Carter, J.P. Kopasz, S. Ahmed, Catal. Today 17 (1–2) (2002) 3.
[7] S. Ahmed, M. Krumpelt, Int. J. Hydrogen Energy 26 (2001) 291.
[8] V.R. Choudhary, A.S. Mamman, S.D. Sansare, Angew. Chem., Int. Ed. Engl. 31 (1992) 1189.
[9] D.A. Hickman, L.D. Schmidt, Science 259 (1993) 343.
[10] D.A. Hickman, L.D. Schmidt, J. Catal. 138 (1992) 267.
[11] Th. Giroux, Sh. Hwang, Y. Liu, W. Ruettinger, L. Shore, Appl. Catal. B: Environ. 55 (2004) 179.
[12] A. Cybulski, J.A. Moulijn (Eds.), Structured Catalysts and Reactors, Chemical Industries, vol. 71, Marcel Dekker, New York, 1998.
[13] J. Chen, Z. Ring, Monolith Catalysts/Reactors and Their Industrial Applications, Hydrocarbon World 2007, 56–58. (http://www.touchbriefings.com/pdf/2447/chen.pdf).
[14] P. Arpentinier, F. Cavani, F. Trifirò, The Technology of Catalytic Oxidations, Editions Technip, Paris, 2001, ISBN 2-7108-0777-7.
[15] L.D. Schmidt, Stud. Surf. Sci. Catal. 130 (2000) 61.
[16] J. Moulijn, A. Stankewicz, F. Kapteijn, Chem. Sustain. Develop. 11 (2003) 3.
[17] R.P. O'Connor, E.J. Klein, L.D. Schmidt, Catal. Lett. 70 (2000) 99.
[18] R.P. O'Connor, E.J. Klein, D. Henning, L.D. Schmidt, Appl. Catal. A: Gen. 238 (2003) 29.
[19] J.R. Rostrup-Nielsen, Catal. Today 71 (2002) 243.
[20] US Department of Energy (DOE), Office of Transportation Technologies, 2001 Annual Progress Report, p. 1.
[21] V.A. Sadykov, T.G. Kuznetsova, S.A. Veniaminov, D.I. Kochubey, B.N. Novgorodov, E.B. Burgina, E.M. Moroz, E.A. Paukshtis, V.P. Ivanov, S.N. Trukhan, S.A. Beloshapkin, Yu.V. Potapova, V.V. Lunin, E. Kemnitz, A. Aboukais, React. Kinet. Catal. Lett. 76 (2002) 83.
[22] N.N. Bulgakov, V.A. Sadykov, V.V. Lunin, E. Kemnitz, React. Kinet. Catal. Lett. 76 (2002) 103.
[23] N.N. Bulgakov, V.A. Sadykov, V.V. Lunin, E. Kemnitz, React. Kinet. Catal. Lett. 76 (2002) 111.
[24] V.A. Sadykov, T.G. Kuznetsova, G.M. Alikina, Y.V. Frolova, A.I. Lukashevich, Y.V. Potapova, V.S. Muzykantov, V.A. Rogov, V.V. Kriventsov, D.I. Kochubei, E.M. Moroz, D.I. Zyuzin, V.I. Zaikovskii, V.N. Kolomiichuk, E.A. Paukshtis, E.B. Burgina, V.V. Zyryanov, N.F. Uvarov, S. Neophytides, E. Kemnitz, Catal. Today 93–95 (2004) 45.
[25] C. Mirodatos, Y. Schuurman, A.C. van Veen, V.A. Sadykov, L.G. Pinaeva, E.M. Sadovskaya, Stud. Surf. Sci. Catal. 167 (2007) 287.
[26] S.N. Pavlova, S.F. Tikhov, V.A. Sadykov, O.I. Snegurenko, Yu.N. Dyatlova, I.A. Zolotarskii, V.A. Kuzmin, L.N. Bobrova, Z.Yu. Vostrikov, Patent Appl. RU 2003130311, 13.10.03.
[27] S. Pavlova, S. Tikhov, V. Sadykov, Y. Dyatlova, O. Snegurenko, V. Rogov, Z. Vostrikov, I. Zolotarskii, V. Kuzmin, S. Tsybulya, Stud. Surf. Sci. Catal. 147 (2004) 223.
[28] S.F. Tikhov, V.V. Usoltsev, V.A. Sadykov, S.N. Pavlova, O.I. Snegurenko, L.L. Gogin, Z.Yu. Vostrikov, A.N. Salanov, S.V. Tsybulya, G.S. Litvak, G.V. Golubkova, O.I. Lomovskii, Stud. Surf. Sci. Catal. 162 (2006) 641.
[29] S. Pavlova, N. Sazonova, V. Sadykov, S. Pokrovskaya, V. Kuzmin, G. Alikina, A. Lukashevich, E. Gubanova, Catal. Today 105 (3–4) (2005) 367.
[30] T.G. Kuznetsova, V.A. Sadykov, E.M. Moroz, S.N. Trukhan, E.A. Paukshtis, V.N. Kolomiichuk, E.B. Burgina, V.I. Zaikovskii, M.A. Fedotov, V.V. Lunin, E. Kemnitz, Stud. Surf. Sci. Catal. 143 (2000) 659.
[31] S.N. Pavlova, N.N. Sazonova, V.A. Sadykov, G.M. Alikina, A.I. Lukashevich, E.L. Gubanova, R.V. Bunina, Stud. Surf. Sci. Catal. 167 (2007) 343.
[32] V. Sadykov, S. Pavlova, Z. Vostrikov, N. Sazonova, E. Gubanova, R. Bunina, G. Alikina, A. Lukashevich, L. Pinaeva, L. Gogin, S. Pokrovskaya, V. Skomorokhov, A. Shigarov, C. Mirodatos, A. van Veen, A. Khristolyubov, V. Ulyanitskii, Stud. Surf. Sci. Catal. 167 (2007) 361.
[33] V.A. Sadykov, S.N. Pavlova, R.V. Bunina, G.M. Alikina, S.F. Tikhov, T.G. Kuznetsova, Yu.V. Frolova, A.I. Lukashevich, O.I. Snegurenko, N.N. Sazonova, E.V. Kazantseva, Y.N. Dyatlova, V.V. Usol'tsev, I.A. Zolotarskii, L.N. Bobrova, V.A. Kuz'min, L.L. Gogin, Z.Y. Vostrikov, Yu.V. Potapova, V.S. Muzykantov, E.A. Paukshtis, E.B. Burgina, V.A. Rogov, V.A. Sobyanin, V.N. Parmon, Kinet. Catal. 46 (2005) 227.
[34] L. Bobrova, I. Zolotarskii, V. Sadykov, S. Pavlova, O. Snegurenko, S. Tikhov, V. Korotkich, T. Kuznetsova, V. Sobyanin, V. Parmon, Chem. Eng. J. 107 (2005) 171.
[35] L. Bobrova, V. Korotkich, V. Sadykov, V. Parmon, Chem. Eng. J. 134 (2007) 145.
[36] L. Bobrova, I. Zolotarsky, V. Sadykov, V. Sobyanin, Int. J. Hydrogen Energy 32 (2007) 3698.
[37] P. Fornasiero, R. Dimonte, G.R. Rao, J. Kaspar, S. Meriani, A. Trovarelli, M. Graziani, J. Catal. 151 (1995) 168.
[38] M.P. Pechini, US Patent 3,330,1967,697.
[39] T. Ishigaki, S. Yamauchi, K. Kishio, J. Mizusaki, K. Fueki, J. Solid State Chem. 73 (1988) 179.
[40] Lj. Kundakovic, M. Flytzani-Stephanopoulos, Appl. Catal. A: Gen. 171 (1998) 13.
[41] Y.H. Hu, E. Ruckenstein, J. Phys. Chem. A 102 (1998) 10568.
[42] P. Avila, M. Montes, E.E. Miŕo, Chem. Eng. J. 109 (2005) 11.
[43] T. Liu, V. Gepert, G. Veser, Chem. Eng. Res. Des. 83 (2005) 611.
[44] G. Veser, in: Y. Wang, J.D. Holladay (Editors), Microreaction Technology and Process Intensification, ACS Symposium Series No. 914, WA, 2005, Chapter 9.
[45] G. Kolios, J. Frauhammer, G. Eigenberger, Chem. Eng. Sci. 55 (2000) 5945.
[46] I.L. Leites, D.A. Sama, N. Lior, Energy 28 (2003) 55.
[47] J.C.H. Li, Ullmann's Encyclopedia of Industrial Chemistry, Wiley-VCH Verlag GmbH & Co. KGaA, 2007.
[48] H.J. Viljoen, N.F.J. van Rensburg, AIChE J. 41 (1995) 1344.
[49] V. Cominos, A. Gavriilidis, Chem. Eng. Sci. 56 (2001) 3455.
[50] V.M. Khanaev, E.S. Borisova, A.S. Noskov, Chem. Eng. Sci. 60 (2005) 5792.
[51] A. Beretta, G. Groppi, L. Majocchi, P. Forzatti, Appl. Catal. A: Gen. 187 (1999) 49.
[52] V.N. Parmon, Russ. J. Phys. Chem. 77 (2003) S128.
[53] M. Pekar, Chem. Eng. Sci. 59 (2004) 4103.
[54] A. Docter, A. Lamm, J. Power Sources 84 (1999) 194.
[55] J.J. Krummenacher, K.N. West, L.D. Schmidt, J. Catal. 215 (2003) 332.
[56] M. Pacheco, J. Sira, J. Kopasz, Appl. Catal. A: Gen. 250 (2003) 161.
[57] A.Q. Clark, S.E. McBsin, J. Kilner, Fluid Phase Equilib. 133 (1997) 239.
[58] R. Schwiedernoch, S. Tischer, C. Correa, O. Deutschmann, Chem. Eng. Sci. 58 (2003) 633.
[59] P.M. Witt, L.D. Schmidt, J. Catal. 215 (2003) 332.
[60] O. Deutschmann, L.D. Schmidt, AIChE J. 44 (1998) 2465.
[61] R.H. Crabtree, Chem. Rev. 95 (1995) 987.
[62] Y.-S. Seo, A. Shiley, S.T. Kolaczkowski, J. Power Sources 108 (2002) 213.
[63] R. Horn, K.A. Williams, N.J. Degenstein, L.D. Schmidt, J. Catal. 242 (2006) 92.
[64] G.R. Schwiedernoch, S. Tischer, C. Correa, O. Deutschmann, Chem. Eng. Sci. 58 (2003) 633.
[65] N.V. Vernikovskaya, L.N. Bobrova, L.G. Pinaeva, V.A. Sadykov, I.A. Zolotarskii, V.A. Sobyanin, I. Buyakou, V. Kalinin, S. Zhdanok, Chem. Eng. J. 134 (2007) 180.
[66] P. Aghalayam, Y.K. Park, N. Fernandes, V. Papavassiliou, A.B. Mhadeshwar, D.G. Vlachos, J. Catal. 213 (2003) 23.
[67] G. Veser, J. Frauhammer, Chem. Eng. Sci. 55 (2000) 2271.
[68] L. Basini, A. Guarinoni, K. Aasberg-Petersen, Stud. Surf. Sci. Catal. 119 (1998) 699.
[69] L. Basini, K. Aasberg-Petersen, A. Guarinoni, M. Østberg, Catal. Today 64 (2001) 9.
[70] G.A. Somorjai, Surf. Sci. 335 (1995) 10.
[71] R.J. Berger, G.B. Marin, Ind. Eng. Chem. Res. 38 (1999) 2582.
[72] Q. Chen, P.M. Couwenberg, G.B. Marin, AIChE J. 40 (1994) 521.